On the track of the brain's microstructure: Myelin water imaging using quantitative MRI

UNI
BASEL

Genehmigt von der Philosophisch-Naturwissenschaftlichen Fakultät

auf Antrag von:

Prof. Dr. Klaus Scheffler
Dissertationsleiter
Prof. Dr. Stefan Ropele
Korreferent

Basel, den 15.11.2011

Prof. Dr. Martin Spiess
Dekan

Abstract

Conventional quantitative magnetic resonance imaging (MRI), for example mono-exponential determination of the relaxation times T_1 and T_2, is sensitive to the various pathologies of myelinated tissue in the brain. However, it gives relatively unspecific information about the underlying nature of the disease. A parameter that directly correlates with the integrity of the myelin sheath is the so-called myelin water fraction (MWF). Based on multi-component analysis of non-invasive quantitative MRI measurements, mapping of the MWF becomes feasible and proved to be useful for studying demyelination and remyelination processes in the course of multiple sclerosis (MS) and other myelin related pathologies.

Common myelin water imaging techniques often suffer from a lack of volume coverage due to their 2D acquisition schemes. This thesis focuses on the development of new myelin water mapping procedures, especially on fast 3D MRI measurements that provide whole brain coverage. In chapter 2, an MWF mapping technique based on balanced steady-state free precession (bSSFP) sequences is introduced. An extended bSSFP signal equation, which is based on a two-pool water model describing brain tissue, is derived to determine typical multi-compartment parameters, including the MWF, of healthy subjects. Possible influences of magnetization transfer effects, finite radiofrequency pulses and B_0/B_1 inhomogeneities are discussed extensively.

Chapter 3 introduces a 3D acquisition scheme based on multi-gradient-echo (mGRE) pulse sequences that is applied for sampling multi-component T_2^* decays in the human brain of healthy volunteers and MS patients. Quantitative myelin water maps are generated based on analysis of T_2^* spectra. Chapter 4 discusses possible adaptations and modifications of the proposed procedure from chapter 3 when moving to higher main magnetic field strengths. The effects of B_0 inhomogeneities on the data sets and possible correction methods are additionally covered in this part of the thesis.

Finally, the crucial role of accurate B_1 and B_0 imaging and the influences on myelin water imaging are revisited in chapter 5. A solution to simultaneous mapping of B_1 and B_0 is presented that might help to overcome systematic error sources in MWF mapping in the future.

List of publications

Journal papers

- **Lenz C**, Klarhöfer M, Scheffler K. Limitations of rapid myelin water quantification using 3D bSSFP. *Magn Reson Mater Phy*, 23:139-151, 2010.

- Sommer G, Klarhöfer M, **Lenz C**, Scheffler K, Bongartz G, Winter L. Signal characteristics of focal bone marrow lesions in patients with multiple myeloma using whole body T_1w-TSE, T_2w-STIR and diffusion-weighted imaging with background suppression. *Eur Radiol*, 21:857-862, 2010.

- **Lenz C**, Klarhöfer M, Scheffler K, Winter L, Sommer G. Assessing extracranial tumors using diffusion-weighted MRI. *Z Med Phys*, 21:79-90, 2011.

- **Lenz C**, Klarhöfer M, Scheffler K. Feasibility of in vivo myelin water imaging using 3D multigradient-echo pulse sequences. *Magn Reson Med*, in press, 2011.

- Smieskova R, Allen P, Simon A, Aston J, Bendfeldt K, Drewe J, Gruber K, Gschwandtner U, Klarhöfer M, **Lenz C**, Scheffler K, Stieglitz RD, McGuire PK, Riecher-Rössler A, Borgwardt SJ. Different duration of at-risk mental state associated with neurofunctional abnormalities - A multimodal imaging study. *Hum Brain Mapp*, in press, 2011.

Conference abstracts

- **Lenz C**, Klarhöfer M, Scheffler K. In vivo myelin water imaging based on balanced steady state free precession. ISMRM White Matter Workshop, Krakow, Poland, 2008, *poster*.

- **Lenz C**, Klarhöfer M, Scheffler K. In vivo myelin water imaging based on balanced steady state free precession. Proceedings of the 25th Annual Meeting ESMRMB, Valencia, Spain, 2008, *poster & oral presentation Highlight Session*.

- **Lenz C**, Klarhöfer M, Scheffler K. In vivo myelin water imaging using z-shimmed multi-gradient-echo pulse sequences. Proceedings of the 17th Annual Meeting ISMRM, Honolulu, USA, 2009, *e-poster*.

- Klarhöfer M, **Lenz C**, Haas T, Scheffler K, Pohmann R. Perfusion measurements during reactive hyperemia in human soleus muscle. Proceedings of the 17th Annual Meeting ISMRM, Honolulu, USA, 2009, *poster*.

- **Lenz C**, Klarhöfer M, Scheffler K, Winter L, Sommer G. Assessing extracranial tumors using diffusion-weighted MRI. Proceedings of the Annual Scientific Meeting SSRMP, Basel, Switzerland, 2009, *oral presentation*.

- Sommer G, Klarhöfer M, **Lenz C**, Scheffler K, Bongartz G, Winter L. Analysis of signal characteristics in T_1w-TSE, T_2w-STIR and diffusion weighted imaging with background suppression (DWIBS) in patients with multiple myeloma. Proceedings of the 26th Annual Meeting ESMRMB, Antalya, Turkey, 2009, *oral presentation*.

- **Lenz C**, Sommer G, Scheffler K, Winter L, Klarhöfer M. Characterization of multicompartmental renal diffusion using a stretched exponential model. Proceedings of the Joint Annual Meeting ISMRM/ESMRMB, Stockholm, Sweden, 2010, *poster*.

- **Lenz C**, Scheffler K, Klarhöfer M. In vivo myelin water imaging using 3D multi-gradient-echo pulse sequences. Proceedings of the Joint Annual Meeting ISMRM/ESMRMB, Stockholm, Sweden, 2010, *oral presentation*.

- Sommer G, Klarhöfer M, **Lenz C**, Scheffler K, Bongartz G, Winter L. Signal behavior of focal bone marrow lesions in patients with multiple myeloma (MM) using T_1w-TSE, T_2w-STIR and diffusion weighted imaging with background suppression (DWIBS). Proceedings of the 22nd Annual Meeting of ESR, Vienna, Austria, 2010, *oral presentation*.

- Sommer G, Klarhöfer M, **Lenz C**, Scheffler K, Bongartz G, Winter L. Signal behavior of focal myeloma lesions in T_1w-TSE, T_2w-STIR and diffusion weighted imaging with background suppression (DWIBS). Proceedings of the 98th Annual Meeting of SSR, Lugano, Switzerland, 2010, *oral presentation.*

- Smieskova R, Allen P, Simon A, Klarhöfer M, Gruber K, **Lenz C**, Blumhagen J, Bendfeldt K, Aston J, Drewe M, Gschwandtner U, Pflueger M, Stieglitz RD, Drewe J, Radue EW, Scheffler K, McGuire PK, Riecher-Rössler A, Borgwardt SJ. High and low probabilities for transition to psychosis associated with neurofunctional abnormalities - A multimodal imaging study. Proceedings of the 7th International Conference on Early Psychosis, Amsterdam, The Netherlands, 2010, *poster.*

- **Lenz C**, Bieri O, Scheffler K, Santini F. Simultaneous B_1 and B_0 mapping using dual-echo actual flip angle imaging (DE-AFI). Proceedings of the 19th Annual Meeting ISMRM, Montreal, Canada, 2011, *e-poster.*

- **Lenz C**, Scheffler K, Klarhöfer M. In vivo myelin water imaging using 3D multi-gradient-echo pulse sequences. 1st International Workshop on MRI Phase Contrast and Quantitative Susceptibility, Jena, Germany, 2011, *poster.*

- Sommer G, Winter L, **Lenz C**, Klarhöfer M, Tamm M, Lardinois D, Forrer F, Bremerich J. Whole body diffusion weighted MRI vs FDG-PET/CT in patients with suspected lung cancer: Initial experience. Proceedings of the 99th Annual Meeting of SSR, Interlaken, Switzerland, 2011, *oral presentation.*

Contents

Chapter 1

Introduction

Magnetic resonance imaging (MRI) is a diagnostic imaging technique that uses the principles of nuclear magnetic resonance (NMR) to obtain high quality structural or functional images from biological tissues. In 1971, Raymond Damadian was the first one who proposed to use MRI as a possible method for the detection of tumors in cancer patients [1]. Two years later, in 1973, the first nuclear magnetic resonance image was published by Paul Lauterbur [2]. However, the introduction to clinical routine became only possible in the early 1980's, when the first vendors started to sell commercial MRI scanners. Since then, MRI became a widely used tool in diagnostics and the modern medical routine would be inconceivable without this imaging technique that benefits from excellent soft tissue contrast and does not expose patients to ionizing radiation.

In general, the contrast of MRI depends on both intrinsic and extrinsic parameters. Intrinsic parameters originate from tissue properties and include the proton density, the relaxation times of the investigated tissue and many others like perfusion, diffusion, temperature, viscosity, chemical environment or magnetization transfer. Extrinsic parameters, on the other hand, relate to the physical characteristics of the MRI system, like the main magnetic field strength, and the acquisition parameters of the applied pulse sequence, as for instance the repetition time, the echo time or the flip angle. By directly controlling the extrinsic parameters, the intrinsic tissue properties can be exploited and the contrast of an MR image can be modified.

In clinical routine, MRI is often used in a purely qualitative way, meaning that diagnoses are based on visual inspection of images acquired at a given set of parameters and interpreting the single contrast. While this approach may perfectly result in the desired information in a short time, it also might suffer from bias, poor reproducibility or misinterpretation due to missing standardization. One possible procedure for circumventing issues connected to qualitative interpretation of MRI data is to perform quantitative analyses. This is usually performed by combining different contrasts that originate from acquisitions based on varying extrinsic parameters (e.g. the echo time) with the aim to directly calculate (respectively quantify) intrinsic parameters, such as the spin-spin relaxation time T_2. Quantitative MRI allows basic physical research and facilitates investigation of biological changes in disease. It especially proved to be of high clinical importance in the field of neurological disease characterization [3]. However, quantitative analysis of MRI data sets requires a longer acquisition time and an often time-consuming off-line computation.

1.1 Multi-component brain tissue characterization

In conventional quantitative MRI, it is assumed that both the longitudinal and transverse components of magnetization relax monoexponentially with specific time constants T_1 and T_2. While this approach holds true for homogeneous samples, the situation in biological tissues is more complex. Physically distinct biological microstructures possess different magnetic resonance properties that give rise to multi-exponential relaxation taking place within one imaging voxel. In its most general form, the signal intensities arising from multi-exponential relaxation can be described by an integral over an exponential kernel [4]:

$$y(t_i) = \int_0^\infty s(\lambda) e^{-\lambda t_i} d\lambda, \tag{1.1}$$

where $s(\lambda)$ is the spectrum from a set of i different experimentally measured values $y(t_i)$ at time t_i.

Brain tissue and especially myelin are of high importance when talking about compartmentalization. Myelin consists of multiple lipid bilayers surrounding the axons of neurons (fig. 1.1) and mainly appears in white matter (WM) and to a small amount as well in gray matter (GM) of the peripheral and central nervous system of vertebrates. Its central function is to increase the velocity of the electrical signal conducted along the axons. The myelin sheath tightly encloses water, which exhibits therefore a shorter transverse relaxation T_2 compared to the intra- and extracellular water of the axon [5–7]. Multi-exponential transverse relaxation can be written as (based on eq. 1.1):

$$y(t_i) = \int_{T_2^{min}}^{T_2^{max}} s(T_2) e^{-t_i/T_2} dT_2, \tag{1.2}$$

where $s(T_2)$ is the amplitude of the corresponding component at relaxation time T_2 and $\int_{T_2} s(T_2) dT_2$ is the total proton density. Quantitative analysis of the multi-component T_2 enables calculation of the fractional pool sizes of the different water compartments in brain tissue. The myelin water fraction (MWF) can then be derived with the help of equation (1.2) according to:

$$MWF = \frac{\int_{T_2^s} s(T_2) dT_2}{\int_{T_2} (T_2) dT_2}, \tag{1.3}$$

with T_2^s representing the T_2 that are attributed to the short water component of brain tissue and hence myelin water.

The short T_2 component of brain tissue was first described by Vasilescu et al. in 1978 [5]. In excised frog sciatic nerve, they found a short T_2 value of 17 ± 6 ms (with 29% fractional pool size) that was associated to water connected to proteins and phospholipids. Moreover, Vasilescu at al. found two additional T_2 compartments:
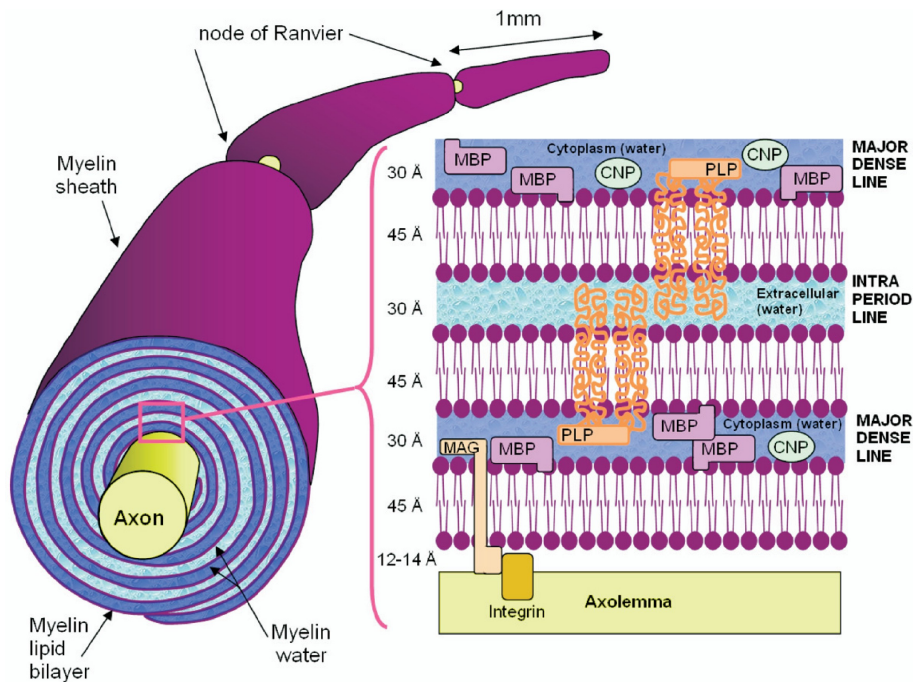
Figure 1.1: *Illustration of the myelin sheath surrounding an axon. Myelin water is tightly enclosed between the myelin bilayers. Inset depicts the lipid bilayer, including myelin basic protein (MBP), proteolipid protein (PLP), cyclic nucleotide phosphodiesterase (CNP) and myelin-associated glycoprotein (MAG). (Source: [8])*

a long one with $T_2 = 310 \pm 21$ ms and 21% contribution and an intermediate one with $T_2 = 70 \pm 14$ ms and corresponding fraction of 50%. The long pool was associated to extracellular water and the intermediate one to axonal water. In 1990 and 1991, two other studies observed a short T_2 peak in vitro. The first one investigated human samples [6], while the second one concentrated on cat brain [7]. Both analyses showed short T_2 values between 10 and 20 ms and corresponding fractions of $7 - 10\%$. In 1994, MacKay et al. first demonstrated the detection of the short T_2 component in humans based on in vivo MRI measurements [9]. They directly attributed this compartment to myelin water and obtained 15% for the averaged myelin water fraction in healthy subjects. In addition, the first in vivo MWF map was published in this early work (fig. 1.2).

Besides the existence of the multi-component T_2 of WM and GM, there is evidence that the longitudinal relaxation T_1 is as well composed of more than one component and that T_1 of myelin water is specifically shorter than T_1 of the intra- and extracellular water pools of the axon [10–13].

The different compartments of brain tissue not only exhibit different relaxation properties, they also undergo a proton exchange that is specified by water molecules diffusing through aquaporin channels of the myelin bilayer [14]. Thereby, the average time a proton remains in one pool before diffusing to the other is described by the mean residence time τ. The timescale of exchange τ is believed to be long
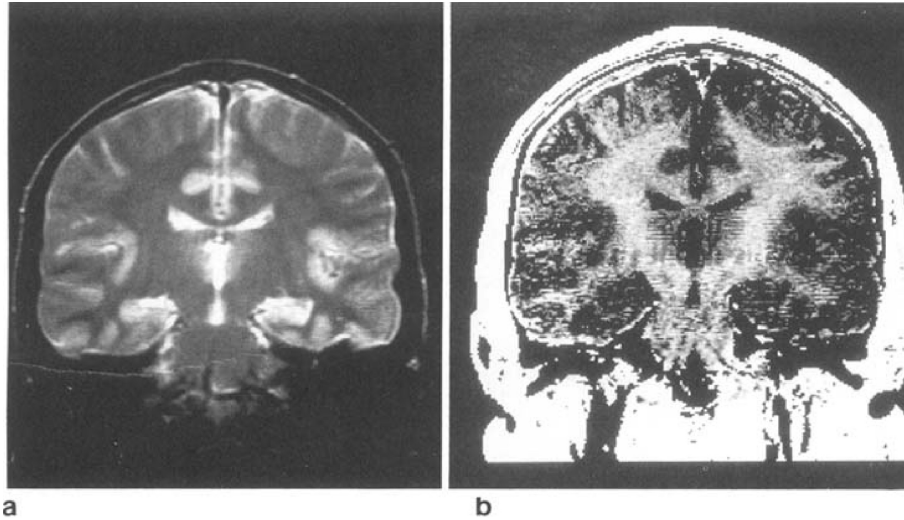
Figure 1.2: *a: Coronal spin-echo image (TE = 60 ms) from the brain of a healthy subject. b: First published myelin water fraction map. (Source: [9])*

on a T_2 timescale ($\tau > 100$ ms), because multiple T_2 components are observed. On the other hand, τ needs to be short on a T_1 timescale ($\tau < 700$ ms), because in conventional T_1 measurements only one component is observed, despite the existence of physically distinct T_1 compartments. The literature value for τ is ~ 200 ms [15–17], which lies between these two limits. As mentioned before, the short timescale of exchange prevents direct observation of multiple T_1 compartments. In order to extract multi-component T_1 information, combined T_1 and T_2 measurements or application of an MRI pulse sequence with combined contrast were shown to be feasible solutions [10–13, 18].

1.2   Why quantifying myelin water?

Common quantitative MRI is sensitive to the various pathologies of myelinated tissue in the brain [3]. However, it gives relatively unspecific information about the underlying nature of the disease. For that reason, a parameter being capable of directly indicating the integrity of the myelin sheath would be highly beneficial for studying neurological diseases. Especially the investigation of multiple sclerosis (MS) could profit from such a quantitative approach, because MS is an autoimmune disease of the central nervous system that is characterized by scattered centers of inflammation and partial or complete loss of myelin in these regions (lesions).

The myelin water fraction is believed to be a parameter that yields direct quantitative information on the myelin sheath integrity. In 2006, Laule et al. demonstrated a strong correlation between the myelin water fraction and the myelin density deduced from histopathological Luxol fast blue myelin stainings (fig. 1.3) [19]. The results of this study and other publications investigating correlations with
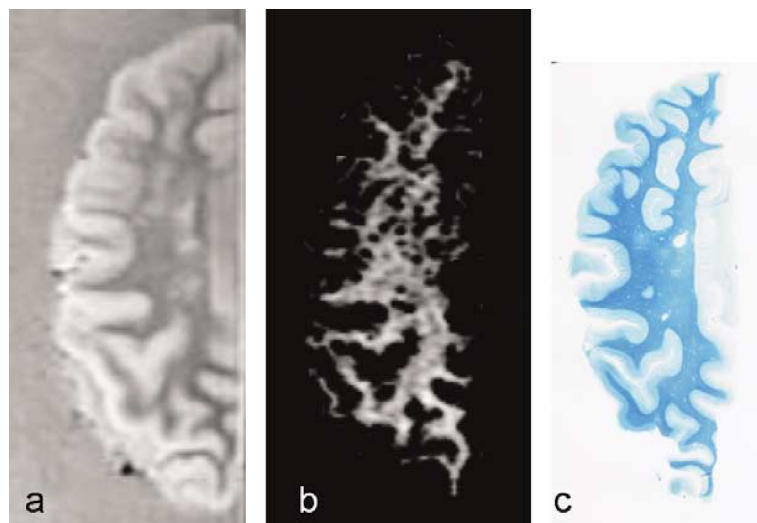
Figure 1.3: *Qualitative correlation between MRI and histopathology of an MS patient. Good qualitative correlation between **a:** spin-echo image (TE = 10 ms) **b:** myelin water map and **c:** Luxol fast blue staining for myelin. (Source: [19])*

histopathology [20–23] strongly support the use of in vivo quantitative myelin water imaging (MWI) for studying myelin pathologies and in particular demyelination, respectively remyelination processes in the course of MS. In the last few years, several studies observing reduced *MWF* in MS lesions were published [9, 13, 19, 21, 22, 24–29]. Moreover, myelin water imaging was used as well for the characterization of other diseases like schizophrenia [30] or phenylketonuria [31], two pathologies connected to dysmyelination, a process that is defined by a defective structure and function of the myelin sheath. Quantitative mapping of myelin water can therefore help to improve the understanding of myelin related diseases and can provide valuable neurological insight that is based on non-invasive MRI measurements.

Besides myelin water imaging, magnetization transfer (MT) [32] imaging is another MRI technique that proved to be directly specific to myelination [33]. In general, MT imaging generates contrast that originates from magnetization exchange between free water and the motionally restricted proton pool arising from non-aqueous, macromolecular tissue like myelin itself. MT experiments can on one side be performed by assessing the magnetization transfer ratio (MTR), where two images are acquired: one with saturation and one without saturation of the macromolecular protons [33]. The MTR is then calculated based on the normalized signal difference of the two images. On the other hand, MT can be assessed by means of quantitative imaging where two-pool characteristics and especially the restricted proton pool fraction are determined [34]. Studies have shown that both the *MWF* and MTR are related to myelin content, but show a relatively weak correlation and indicate different processes of demyelinating diseases [20, 24, 26, 29, 35]. In particular, the MTR and the restricted pool fraction are believed to change due to inflammation processes, whereas the *MWF* stays unaffected in this context

[20, 24, 26, 29], thereby indicating that both techniques, myelin water imaging and MT imaging, provide largely independent measures of myelin related pathologies.

1.3 Myelin water imaging and analysis techniques

1.3.1 Multi-spin-echo based myelin water quantification

When MacKay et al. published the first in vivo myelin water map in 1994 [9], they were most probably not conscious about the fact that they would also introduce the future 'gold standard' for myelin water acquisition within this article. In this first work and in the subsequent study [36], acquisition of brain T_2 decay was performed by using a single-slice 32-echo spin-echo pulse sequence with a slice-selective 90° pulse and rectangular 180° refocusing pulses. Moreover, a series of slice-select crusher gradients with alternating sign and decreasing amplitude was implemented around the 180° refocusing pulses to eliminate contributions from stimulated echoes and non-perfect slice profiles (fig. 1.4) [36, 37]. In all succeeding publications applying this technique, composite 180° pulses (90_x - 180_y - 90_x) based on the Carr-Purcell-Meiboom-Gill condition were used that resulted in improved suppression of stimulated echoes and provided more reliable in vivo results [3, 38, 39]. The typical sequence parameters used for myelin water imaging were $TR = 3$ s, echo spacing = 10 ms, ~ 4 averages and a total scan time between 20 and 25 minutes for the single-slice 32-echo acquisition.

The obtained T_2 decay curves (fig. 1.5a) were analyzed by assuming a multi-exponential composition of T_2 relaxation based on an arbitrary number of components (valid for $TR \gg T_1$):

$$y_i = \sum_{k=1}^{M} s_k exp(-t_i/T_{2k}), \ i = 1, 2, ..., N,$$ (1.4)

where t_i are the N measured echo times, T_{2k} are M logarithmically spaced T_2 relaxation times and s_k is the relative amplitude for each corresponding T_2 relaxation time. This equation is only valid for long TR, where potential (multi-compartment) T_1 influences can be neglected. For the fitting of the multi-exponential data, a non-negative least-squares algorithm (NNLS) was applied [40, 41]. NNLS is a non-iterative, linear algorithm that does neither require initial conditions nor a-priori knowledge about the number of components. When using NNLS, a large number of T_{2k} relaxation times is fixed and only s_k is treated as unknown, yielding finally non-negative s_k with a majority of s_k being equal to zero. In detail, χ^2, the misfit between the measured and predicted data is minimized:

$$\chi^2 = \sum \left(y_i - \mathbf{A}s\right)^2, \ A_{ik} = exp(-TE_i/T_{2k}).$$ (1.5)
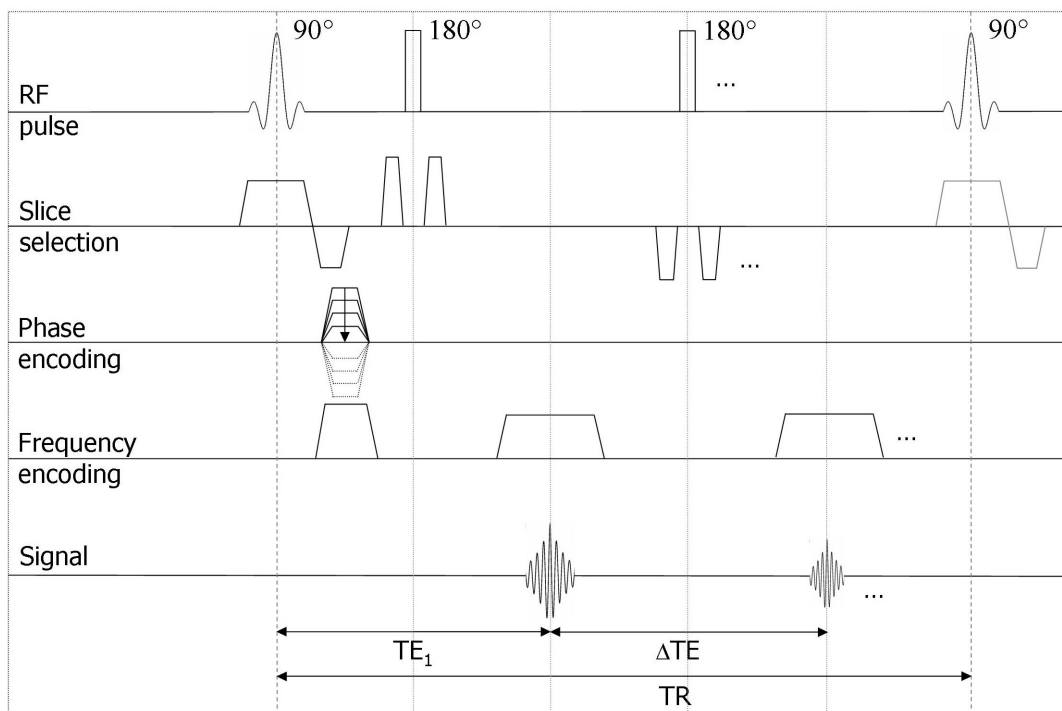
Figure 1.4: *Sequence diagram of a multi-spin-echo pulse sequence with pairs of slice-select crusher gradients having alternating signs and decreasing amplitudes [37], as it is used for conventional myelin water quantification.*
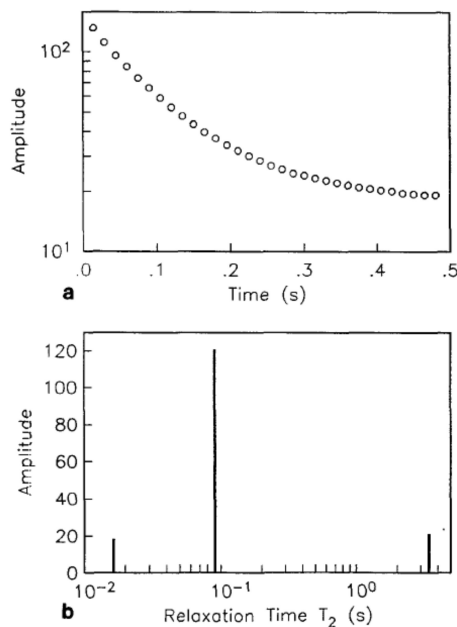
Figure 1.5: *a:* T_2 *decay curve from a volume of interest in normal human brain acquired in vivo.* *b:* T_2 *relaxation distribution from the decay curve in a. The three components are assigned to: myelin water with* T_2 *between 10 and 55 ms, intra- and extracellular water with* T_2 *between 70 and 95 ms and cerebrospinal fluid with* T_2 *greater than 1 s. (Source: [9])*

The final solution is then a set with a few non-zero discrete peaks (fig. 1.5b).

In later publications [36], both χ^2 and an additional energy constraint, smoothing the T_2 distribution, were minimized:

$$\chi^2 + \mu \sum_{k=1}^{M} s_k^2, \ \mu \geq 0. \tag{1.6}$$

In general, the larger the μ parameter, the smoother the T_2 distribution becomes at the cost of misfit. Regularized distributions could be achieved by applying the following limits to the energy constraint:

$$1.02\chi_{min}^2 \leq \chi^2 \leq 1.025\chi_{min}^2. \tag{1.7}$$

This modification provided more consistent fits in the presence of noise [40–42]. The *MWF* finally was defined as the sum of the amplitudes s_k with T_2 relaxation times between 10 and 50 ms relative to the total sum of all amplitudes.

As mentioned previously, the procedure proposed by MacKay et al. was successfully used for the investigation of demyelinating processes in the course of MS and is, until today, the most commonly used technique for myelin water imaging [9, 19, 22, 24–26, 28, 29]. Recently, this technique was applied as well for studying myelin water not only in the brain, but also in the spinal cords of animal models [35, 43, 44].

Nevertheless, there are some drawbacks associated to this myelin water quantification approach. First of all, an average of four scans is usually needed to achieve an adequate signal-to-noise ratio (SNR) for data analysis, hence leading to an increased scan time of ~ 20 minutes. The long acquisition time and the lack of volume coverage due to the single-slice technique severely impair the implementation in daily clinical routine. Furthermore, shortening of the first echo time and the echo spacing is hindered in the sequence scheme, because of the relatively long durations of the refocusing pulses and the crusher gradients. This issue can result in a significant loss of portions of the myelin water signal and impair an accurate sampling of the short T_2 decay. In addition, there is no possibility to directly assess the proton exchange between the two T_2 compartments with the multi-spin-echo procedure. Although it was shown that intercompartmental exchange does not drastically alter the amplitudes and positions of the T_2 components [12, 16, 45], quantifying exchange might still help to understand disease processes in more detail and a direct assessment would therefore be highly attractive.
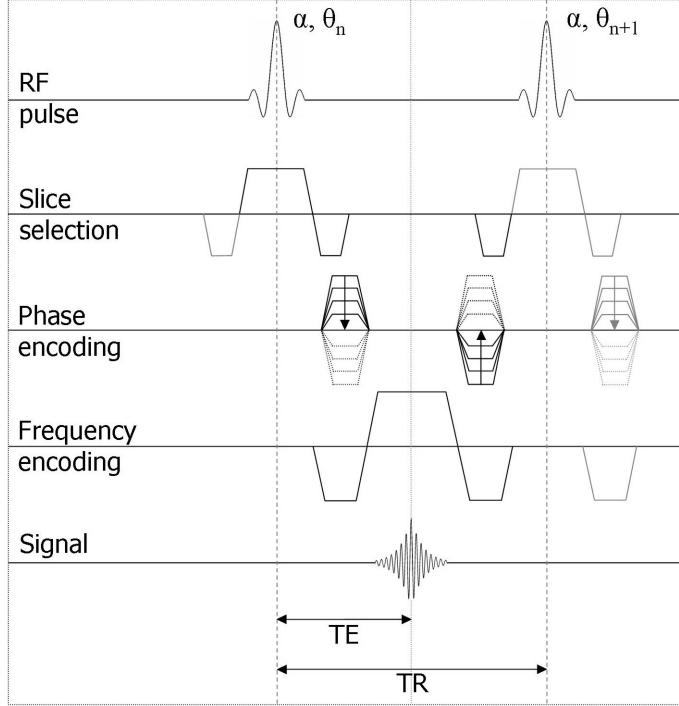
Figure 1.6: *Sequence diagram of a balanced SSFP pulse sequence. On all the three gradient axes, the net gradient area equals zero within one TR interval.*

1.3.2　Myelin water quantification based on balanced SSFP

The application of balanced steady-state free precession (bSSFP) pulse sequences offers the possibility to overcome the main limitations of myelin water imaging based on conventional multi-spin-echo pulse sequences. Imaging with 3D bSSFP benefits from very short acquisition times (about 2 minutes for one 3D data set), high resolution and excellent SNR [46]. BSSFP delivers the highest signal amplitude of all SSFP sequences. It is in principle a rapid gradient-echo pulse sequence that is characterized by a short repetition time and a complete nulling of all gradient areas on the three gradient axes within one repetition time, meaning that the gradient-induced dephasing within TR is exactly zero (fig. 1.6). Because of the short TR ($TR < T_2$, $TR \ll T_1$), the longitudinal magnetization can not relax back to thermal equilibrium and the transverse magnetization does not return to zero before each new excitation. Under these conditions and after a certain number of excitations, a dynamic equilibrium or steady state builds up that leads to a periodic magnetization (valid for all types of SSFP) [47]. Using partial integration of the Bloch equations [48], the steady state of bSSFP can be derived analytically [49, 50] yielding:

$$S(\alpha, T_1, T_2, TR) = M_0 \sin\alpha \frac{(1 - E_1)\sqrt{E_2}}{1 - E_1 E_2 - (E_1 - E_2)\cos\alpha}. \tag{1.8}$$

This equation is valid for centered echoes ($TE = TR/2$) and alternating excitations ($\pm\alpha$). Furthermore, $E_{1,2} = exp(-TR/T_{1,2})$ and M_0 is the equilibrium magnetization. The contrast of bSSFP is therefore a composition of T_1 and T_2 contributions at the same time. For sufficiently small repetition times ($TR \ll T_1, T_2$), the steady-state signal becomes proportional to T_2/T_1 [51].

Equation (1.8) is only valid for a single water compartment. However, under certain assumptions, it is possible to solve the steady state of bSSFP for the case of multi-component systems. In chapter 2, a complete mathematical derivation of an extended bSSFP signal equation will be presented, in order to characterize the bSSFP behavior of the different water pools in brain tissue. The resulting two pool bSSFP equation is not only a function of the relaxation times of the water compartments and the myelin water fraction, but also proton exchange is incorporated. Based on multiple 3D bSSFP acquisitions with varying flip angle and application of the extended bSSFP equation as fit equation, high resolution myelin water imaging with whole brain coverage becomes feasible in a clinically reasonable measurement time of 20 minutes (chapter 2).

Recently, also Deoni et al. made use of the strong benefits of bSSFP for quantitative myelin water imaging. In contrast to the work presented in chapter 2 of this thesis, Deoni et al. not only applied bSSFP sequences, but also spoiled gradient-echo (SPGR) pulse sequences [13]. SPGR is an SSFP sequence that is characterized by a dephasing moment in readout direction and a spoiler gradient applied on the slice select axis to destroy any remaining transverse magnetization [52]. Additionally, radiofrequency (RF) spoiling schemes are used to further reduce transverse coherences [53]. Deoni et al. solved the two-pool steady-state signal for both bSSFP and SPGR. 3D bSSFP and SPGR measurements with varying flip angle were acquired in healthy subjects and MS patients with a total scan time of 30 minutes for a resolution of 1 x 1.4 x 1.4 mm^3. By using a complex hybrid approach consisting of a genetic algorithm [54] and a local search method [55], all parameters describing the two-pool brain tissue model could be extracted (fig. 1.7). The resulting averaged *MWF* value for healthy WM was 29.5% [13], which is the highest myelin water fraction observed up to now. Possible explanations for the high results could be influences of B_0 and B_1 inhomogeneities or MT effects that impair an accurate detection of myelin water (for an extensive discussion of these effects and their influences on myelin water imaging based on bSSFP sequences, see chapter 2). The myelin water imaging technique proposed by Deoni et al. was lately successfully applied in a comprehensive MS study [56] and was as well used to investigate the *MWF* in the spinal cord [57].
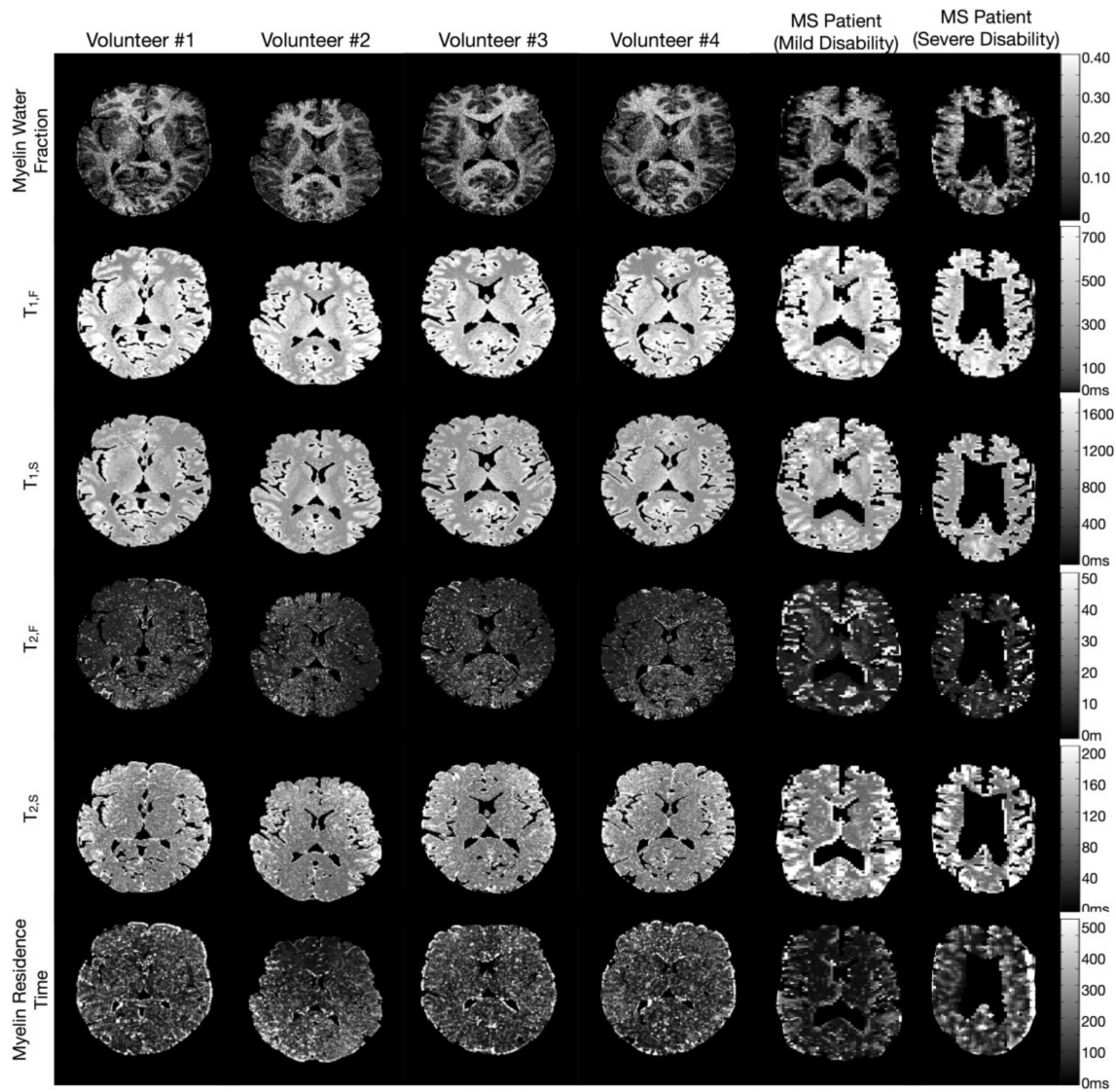
Figure 1.7: *Representative axial slices showing the myelin water fraction, the myelin residence time and the corresponding multi-component relaxation time maps from four healthy volunteers and two MS patients. (Source: [13])*
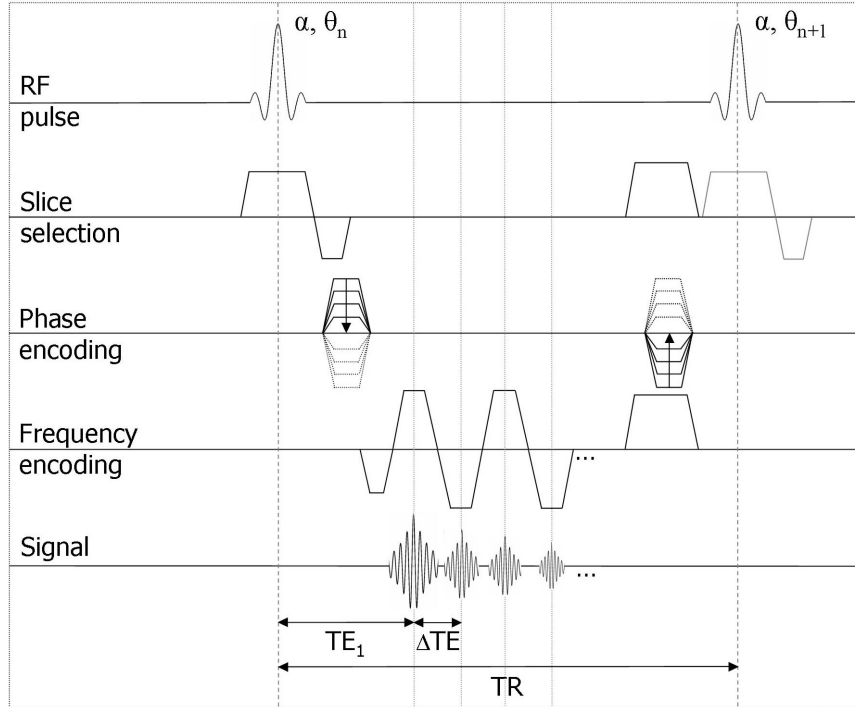
Figure 1.8: *Sequence diagram of a multi-gradient-echo pulse sequence with alternating readout gradient polarities, as it is used for myelin water quantification based on multi-component T_2^* decay.*

1.3.3   Multi-gradient-echo based myelin water quantification

Du et al. lately introduced another new myelin water quantification method with great potential for overcoming the main issues related to the conventional multi-spin-echo procedure. They proved that not only multi-component T_2 decay, but also T_2^* relaxation can be used for deriving the *MWF* [21]. In the course of their study, a 2D multi-gradient-echo (mGRE) pulse sequence with alternating readout gradient polarities and 126 different echo times (fig. 1.8) was used to acquire the brain T_2^* decay in one post-mortem brain with MS. The total scan time for 5 slices at field strength of 3 T was below 9 minutes. The application of mGRE pulse sequences benefits from a short first echo and echo spacing, thereby enabling a precise sampling of the myelin water signal. Du et al. could successfully reduce the first echo to 2.1 ms and the echo spacing to 1.1 ms. With this setup, the myelin water signal with a T_2^* of ~ 10 ms was 81% at the first echo and still 24% at the 12th echo. The resulting myelin water fraction maps from the post-mortem brain were correlated with histophathological results from Luxol fast blue myelin stainings, which confirmed the observed demyelination within MS lesions in the *MWF* maps and verified the proposed procedure based on T_2^* relaxation analysis (fig. 1.9).

The majority of the existing myelin water imaging studies based on multi-spin-echo sequences apply an NNLS algorithm to analyze the T_2 data curves. This approach
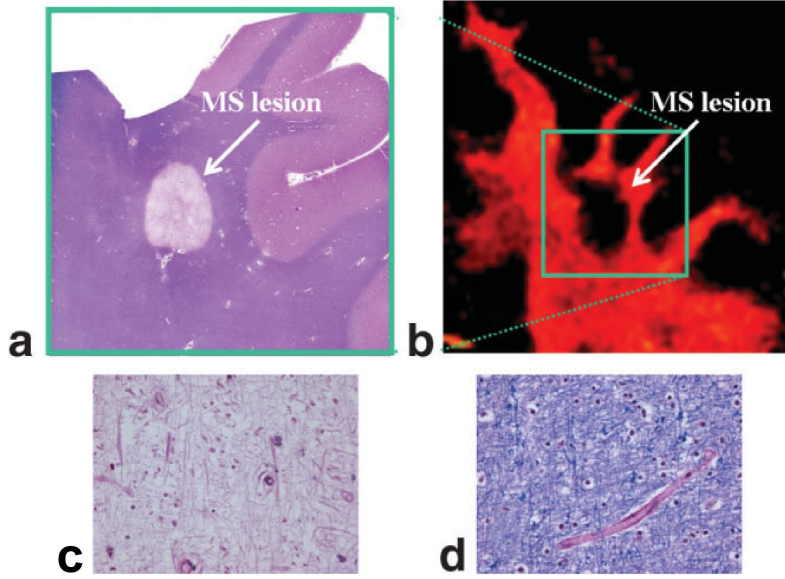
Figure 1.9: *a: Histopathology of an MS lesion confirming the demyelination within the investigated lesion. b: Corresponding MWF map (derived from multi-component T_2^* analysis) showing severely decreased intensity at the position of the MS lesion. A higher-power photomicrograph demonstrates the total devoid of myelin at the center of the MS lesion (c) and the normal myelin content in normal appearing white matter outside the lesion (d). (Source: [21])*

benefits from not requiring initial assumptions about the number of components present. In contrast to the conventional procedure, Du et al. used a fixed three-pool model for data analysis where the intra- and extracellular compartments are separated [21, 58, 59]. The main advantage of the three-pool model is the additional insight into the axonal integrity that is provided by fitting the axonal water independently of the extracellular component. Nevertheless, a higher number of components will always deliver superior fit results, not necessarily because of the physical existence of these compartments, but because of the higher probability to match the curve more accurately with more unknowns. Therefore, if possible, the NNLS algorithm should be favored over the application of a fixed model.

The technique proposed by Du et al. could in the meanwhile successfully be applied to in vivo measurements of healthy subjects [60]. However, the procedure still lacks an adequate volume coverage because of the acquisition of only a few slices. In chapter 3 of this thesis, a new approach based on 3D mGRE pulse sequences will be presented that offers whole brain coverage and uses NNLS algorithms for the analysis of in vivo multi-component brain T_2^* relaxation from healthy volunteers and MS patients.

1.4   Aim of this thesis

As mentioned above, quantitative myelin water imaging proved to be of high clinical importance for the characterization of neurological diseases due to the direct correlation between the myelin water fraction and the integrity of the myelin sheath. Especially the investigation of multiple sclerosis benefits from deriving the myelin water fraction, because quantitative insight into changes within MS lesions and overall changes in white matter of MS patients can be gained.

However, most of the existing myelin water imaging methods are still not suitable for the daily clinical routine. Major drawbacks are the lack of volume coverage due to the 2D acquisition schemes and the long MRI acquisition times. In particular the 'gold standard', where multi-spin-echo sequences are applied, suffers from these issues. Additionally, long first echo times and echo spacings are further limitations of the multi-spin-echo procedure. This can lead to a significant loss of portions of the myelin water signal and impair an accurate sampling of the short T_2 decay.

In this thesis, new techniques are presented that aim to overcome the major issues of common myelin water imaging procedures. The principal target is thereby the shortening of the acquisition time and the coverage of the whole brain by using 3D MRI pulse sequences. One part of this thesis focuses on the application of 3D bSSFP sequences that offer a high resolution, high signal-to-noise ratios and very short scan times (approximately 2 minutes for one 3D data set). In order to assess the *MWF* with this technique, an extended bSSFP signal equation is developed that is based on a two-pool water model describing white and gray matter of brain tissue. Another possibility for improving the detection of the short myelin water pool is using 3D multi-gradient-echo pulse sequences, the second main area of the present thesis. 3D mGRE sequences profit not only from their fast acquisition times (less than 10 minutes for the acquisition of 96 echoes), but also from their short first echo times and echo spacings, which enable accurate sampling of T_2^* decay curves.

In the course of this thesis, the novel methods are presented and their applicability in a real clinical environment is intensely tested by incorporating in vivo measurements of healthy volunteers and MS patients. Moreover, possible influences that impair reliable myelin water detections are discussed in detail and solutions to circumvent limitations are proposed in the following chapters of this work.

1.5   Outline of the thesis

In chapter 2, an *MWF* mapping technique using 3D balanced steady-state free precession sequences is implemented. An extended bSSFP signal equation, which is based on a two-pool water model describing brain tissue, is derived to determine typical multi-compartment parameters, including proton exchange and most importantly the *MWF*. Numerical simulations of the modified Bloch equations are performed to confirm the assumptions made in the course of the derivation and to validate the two-pool bSSFP signal equation. The new signal equation is then used to analyze data from in vivo 3D bSSFP measurements with varying flip angles of healthy human brains. The *MWF* and the signal amplitude are fitted as single unknowns, while keeping the remaining parameters of the two-pool system (relaxation times of the two pools and exchange rate) fixed. Both region of interest and pixelwise results from healthy subjects are presented. The effect of variation of the relaxation times and the exchange rate on the *MWF* estimation is discussed. Moreover, the influence of finite RF pulses and magnetization transfer, as well as the dependence on B_0 and B_1 inhomogeneities are carefully investigated in this chapter.

Chapter 3 introduces a 3D measurement scheme based on multi-gradient-echo pulse sequences that is applied for the sampling of multi-component T_2^* decays by acquiring signals at 96 different echo times. Quantitative myelin water maps are generated based on analysis of T_2^* spectra and their corresponding amplitudes. Both healthy subjects and patients suffering from multiple sclerosis are investigated with the proposed technique. Furthermore, the influence of B_0 inhomogeneities on the derived myelin water maps and other effects that can possibly alter the obtained *MWF* values are discussed in this chapter.

Possible adaptations and modifications of the proposed procedure from chapter 3 are covered in chapter 4. This part of the thesis mainly focuses on measurements performed at higher field strengths and their resulting consequences due to stronger B_0 inhomogeneities. Several pathways for circumventing B_0 issues, like z-shimming, are delineated in this chapter. The crucial role of accurate B_1 and B_0 imaging and the influences on myelin water imaging are finally revisited in chapter 5. A solution to simultaneous mapping of B_1 and B_0 based on dual-echo actual flip angle imaging is presented that might help to overcome systematic error sources in *MWF* mapping in the future.

Chapter 2

Myelin water imaging using 3D bSSFP pulse sequences

2.1 Introduction

Based on the idea that bSSFP sequences [61] can successfully be used for the quantitative assessment of magnetization transfer [62], this chapter introduces the application of bSSFP for the quantification of myelin water. Imaging with bSSFP benefits from very short acquisition times (about 2 min for one 3D data set), high resolution and excellent signal-to-noise ratio (SNR) [46]. The signal formation in bSSFP is usually described by the Freeman-Hill formulae [49, 50]. However, in most biological tissues like WM or GM, the signal is more completely described by a complex composition of relaxation instead of the classical single-pool behavior, as described in chapter 1. In this part of the thesis, a complete mathematical derivation of an extended bSSFP signal equation, based on a two-pool water model describing WM and GM, is presented. The model consists of a short pool (myelin water, abbreviation s), a long pool (extracellular and axonal water, abbreviation l) and additionally includes proton exchange between the pools. The extended bSSFP signal equation is a function of the repetition time TR, the echo time TE, the flip angle α, the relaxation times of the two pools (T_2^s, T_2^l, T_1^s, T_1^l), the exchange rate k and most importantly the MWF.

The two-pool bSSFP signal equation is validated by numerical simulations of the full set of non-simplified ordinary differential equations (ODE). Moreover, the influence of finite RF pulses and MT, as well as the dependence on B_0 and B_1 inhomogeneities are carefully investigated in this part of the thesis. The new signal equation is used to fit data from in vivo 3D bSSFP measurements with varying flip angle. The MWF and the signal amplitude are fitted as single unknowns, while keeping the remaining parameters of the two-pool system (relaxation times of the two pools and exchange rate) constant. Both region of interest (ROI), and pixel-wise results from the fitting of axial, sagittal and coronal views of healthy subjects are presented. The effect of variation of the relaxation times and the exchange rate on the MWF fit is discussed.

2.2 Theoretical background

2.2.1 Conventional bSSFP signal equation

In the case of a single water compartment, the steady state of bSSFP is derived from the Bloch equations using partial integration [49, 50], resulting in:

$$S(\alpha, T_1, T_2, TR) = M_0 \sin \alpha \frac{(1 - E_1)\sqrt{E_2}}{1 - E_1 E_2 - (E_1 - E_2)\cos \alpha}. \tag{2.1}$$

This equation is valid for centered echoes ($TE = TR/2$) and alternating excitations ($\pm \alpha$). Furthermore, $E_{1,2} = exp(-TR/T_{1,2})$ and M_0 is the equilibrium magnetiza-

tion. For WM and GM, which are complex biological tissues, the bSSFP signal is more accurately described by a complex composition of relaxation instead of the classical single-pool behavior. In the following, a complete mathematical derivation of an extended bSSFP signal equation will be presented, in order to characterize the bSSFP behavior of the different water pools in brain tissue. For the mathematical derivation a similar nomenclature as in references [13] and [63] is used.

2.2.2   Two-pool water model

To accurately describe the bSSFP signal of WM and GM, a theoretical two-pool model is used. The short pool consists of myelin water, whereas the extracellular and the axonal water are combined to the long pool. The relaxation times T_1^s and T_2^s belong to the short pool, T_1^l and T_2^l to the long one (fig. 2.1). Furthermore, the two components undergo a proton exchange that is indicated by the exchange rates k_{sl} and k_{ls}. Exchange is specified by water molecules diffusing through aquaporin channels [14] of the myelin bilayer either from the short to the long pool (k_{sl}) or vice versa (k_{ls}). The exchange rates are the reciprocals of the mean residence times τ_{sl} and τ_{ls}, the average time a proton remains in one pool before diffusing to the other. In kinetic equilibrium, the two exchange rates are related through the fractional pool sizes by $k_{sl} = (MWF^{-1} - 1)k_{ls}$. The MWF stands for the molar fraction of the short pool and is defined as $MWF = M_0^s/(M_0^s + M_0^l)$, where M_0^s (M_0^l) denotes the equilibrium magnetization of the short (long) pool. Aside from that, a general exchange rate can be defined as $k = k_{sl} + k_{ls}$, whereby $k_{sl} = (1 - MWF) \cdot k$ and $k_{ls} = MWF \cdot k$ become valid. The timescale of exchange τ is believed to be long on a T_2 timescale ($\tau > 100ms$), because two T_2 components are observed. On the other hand, τ needs to be short on a T_1 timescale ($\tau < 700$ ms), because in conventional T_1 measurements only one component is observed, despite the existence of two physically different T_1. The literature value for τ is ~ 200 ms [15–17], which lies between the two limits and corresponds to $k \sim 5 \ s^{-1}$.
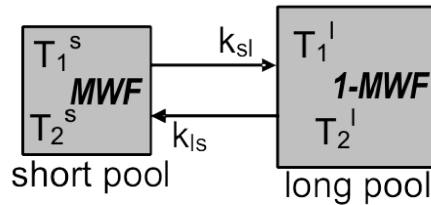

Figure 2.1: *Physical properties of the two water pools describing WM and GM. The short pool has relaxation times T_1^s, T_2^s and the fractional pool size MWF, whereas T_1^l, T_2^l and (1-MWF) belong to the long pool. Proton exchange is described by the two exchange rates k_{sl} and k_{ls}.*

2.2.3 Modified Bloch equations

The magnetization of the short pool will decrease by the factor $k_{sl}\mathbf{M}^s$ and increase by $k_{ls}\mathbf{M}^l$, if exchange between the two pools occurs. On the other hand, the magnetization of the long pool will rise by $k_{ls}\mathbf{M}^l$ and decrease by $k_{sl}\mathbf{M}^s$. This leads to modified 6-dimensional Bloch equations [48], which describe all spatial components of the two-pool magnetization vector $\mathbf{M} = [M_x^s, M_x^l, M_y^s, M_y^l, M_z^s, M_z^l]$ separately:

$$\frac{dM_x^s}{dt} = \omega_0 M_y^s - \frac{M_x^s}{T_2^s} - k_{sl}M_x^s + k_{ls}M_x^l, \tag{2.2a}$$

$$\frac{dM_x^l}{dt} = \omega_0 M_y^l - \frac{M_x^l}{T_2^l} - k_{ls}M_x^l + k_{sl}M_x^s, \tag{2.2b}$$

$$\frac{dM_y^s}{dt} = -\omega_0 M_x^s - \frac{M_y^s}{T_2^s} - k_{sl}M_y^s + k_{ls}M_y^l + \omega_1(t)M_z^s, \tag{2.2c}$$

$$\frac{dM_y^l}{dt} = -\omega_0 M_x^l - \frac{M_y^l}{T_2^l} - k_{ls}M_y^l + k_{sl}M_y^s + \omega_1(t)M_z^l, \tag{2.2d}$$

$$\frac{dM_z^s}{dt} = \frac{M_0^s - M_z^s}{T_1^s} - k_{sl}M_z^s + k_{ls}M_z^l - \omega_1(t)M_y^s, \tag{2.2e}$$

$$\frac{dM_z^l}{dt} = \frac{M_0^l - M_z^l}{T_1^l} - k_{ls}M_z^l + k_{sl}M_z^s - \omega_1(t)M_y^l. \tag{2.2f}$$

Here, M_s^0 (M_l^0) is again the abbreviation for the equilibrium magnetization of the short (long) pool, $\omega_0 = \gamma\,|\mathbf{B}_0|$ and $\omega_1(t) = \gamma\,|\mathbf{B}_1(t)|$. Moreover, it is assumed that $\omega_0 = \omega_0^s = \omega_0^l$. The modified Bloch equations describe the cases of excitation, relaxation and exchange.

2.2.4 Solutions to the modified Bloch equations

Although, it may in principle be possible to solve the system of differential equations (eqs. 2.2a-f), the solution is complex and cumbersome. Therefore, a different procedure is suggested, which closely follows the vector model description introduced by Carr [47] to derive the signal behavior of bSSFP. To separate excitation and relaxation, instantaneously acting RF pulses are assumed. Using the matrix notation developed by Jaynes [64], the solution for excitation is written as a rotation around the x-axis (without loss of generality):

$$\mathbf{M}_n^+ = \mathbf{R}_x(\alpha)\mathbf{M}_n^- = \begin{bmatrix} 1 & 0 & 0 & 0 & 0 & 0 \\ 0 & 1 & 0 & 0 & 0 & 0 \\ 0 & 0 & \cos\alpha & 0 & \sin\alpha & 0 \\ 0 & 0 & 0 & \cos\alpha & 0 & \sin\alpha \\ 0 & 0 & -\sin\alpha & 0 & \cos\alpha & 0 \\ 0 & 0 & 0 & -\sin\alpha & 0 & \cos\alpha \end{bmatrix} \mathbf{M}_n^-, \tag{2.3}$$

where α is the flip angle and $\mathbf{M}_n^-$ is the 6-dimensional magnetization vector before the nth RF pulse. The solution for relaxation is found analogously to the 3-dimensional classical case [49, 50]. The resulting relaxation matrix is given by:

$$\mathbf{E}(t) = \begin{bmatrix} E_2^s & 0 & 0 & 0 & 0 & 0 \\ 0 & E_2^l & 0 & 0 & 0 & 0 \\ 0 & 0 & E_2^s & 0 & 0 & 0 \\ 0 & 0 & 0 & E_2^l & 0 & 0 \\ 0 & 0 & 0 & 0 & E_1^s & 0 \\ 0 & 0 & 0 & 0 & 0 & E_1^l \end{bmatrix}, \tag{2.4}$$

where $E_{1,2}^s = exp(-t/T_{1,2}^s)$, $E_{1,2}^l = exp(-t/T_{1,2}^l)$.

To solve the modified Bloch equations for exchange, it is additionally assumed that exchange processes decouple from relaxation processes within the short repetition times usually applied in bSSFP imaging. This approach is valid, as long as fractional pool size modifications from longitudinal relaxation processes are negligible within TR. This corresponds to an instantaneous appearance of exchange, similar to the concept of instantaneous rotation allowing the decoupling of excitation and relaxation. The part of the modified Bloch equations containing only exchange parameters reads:

$$\frac{d\mathbf{M}}{dt} = \begin{bmatrix} -k_{sl} & k_{ls} & 0 & 0 & 0 & 0 \\ k_{sl} & -k_{ls} & 0 & 0 & 0 & 0 \\ 0 & 0 & -k_{sl} & k_{ls} & 0 & 0 \\ 0 & 0 & k_{sl} & -k_{ls} & 0 & 0 \\ 0 & 0 & 0 & 0 & -k_{sl} & k_{ls} \\ 0 & 0 & 0 & 0 & k_{sl} & -k_{ls} \end{bmatrix} \mathbf{M}. \tag{2.5}$$

This differential equation has the general solution $\mathbf{M}(t) = \mathbf{A}(t)\mathbf{M}_0$, where $\mathbf{A}(t)$ is the exchange matrix:

$$\mathbf{A}(t) = \begin{bmatrix} a & b & 0 & 0 & 0 & 0 \\ c & d & 0 & 0 & 0 & 0 \\ 0 & 0 & a & b & 0 & 0 \\ 0 & 0 & c & d & 0 & 0 \\ 0 & 0 & 0 & 0 & a & b \\ 0 & 0 & 0 & 0 & c & d \end{bmatrix}, \tag{2.6}$$

where

$$a = -(MWF - 1)e^{-kt} + MWF,$$
$$b = -MWF(e^{-kt} - 1),$$
$$c = (MWF - 1)(e^{-kt} - 1),$$
$$d = MWF(e^{-kt} - 1) + 1.$$

k_{sl} and k_{ls} were replaced by the corresponding expressions including k and MWF. Although the concatenation of relaxation and exchange is not a general solution

for longer TR, it can be applied in the limit of short TR. The limit of $TR \to 0$ leads to the case of commuting relaxation and exchange matrices:
$[\mathbf{E}(TR \to 0), \mathbf{A}(TR \to 0)] \to 0$.

2.2.5   Extended bSSFP signal equation

The extended steady-state equation can now be derived according to standard procedures [51] with the solutions for excitation, relaxation and exchange from above. RF phase alternations are described by $\mathbf{R}_z$:

$$\mathbf{R}_z(\Phi = 180°) = \begin{bmatrix} -1 & 0 & 0 & 0 & 0 & 0 \\ 0 & -1 & 0 & 0 & 0 & 0 \\ 0 & 0 & -1 & 0 & 0 & 0 \\ 0 & 0 & 0 & -1 & 0 & 0 \\ 0 & 0 & 0 & 0 & 1 & 0 \\ 0 & 0 & 0 & 0 & 0 & 1 \end{bmatrix}. \tag{2.7}$$

For bSSFP, the magnetization directly after the nth RF-pulse yields
$\mathbf{M}_n^+ = \mathbf{R}_z \mathbf{R}_x(\alpha) \mathbf{M}_n^-$, where $\mathbf{M}_n^-$ is the magnetization before the nth RF-pulse. The magnetization before the $(n+1)^{th}$ pulse yields (assuming relaxation takes place before exchange):

$$\mathbf{M}_{n+1}^- = \mathbf{A}(TR) \left[\mathbf{E}(TR)\mathbf{M}_n^+ + \mathbf{M}_0 \right], \tag{2.8}$$

with the equilibrium magnetization given by:

$$\mathbf{M}_0 = \begin{bmatrix} 0 \\ 0 \\ 0 \\ 0 \\ M_0^s(1 - E_1^s) \\ M_0^l(1 - E_1^l) \end{bmatrix}. \tag{2.9}$$

In steady state, the eigenvalue equation takes the form $\mathbf{M}_n^- = \mathbf{M}_{n+1}^-$ and the final result becomes (for centered echoes with $TE = TR/2$ and the case relaxation before exchange):

$$\mathbf{M}_n^+(\infty) = \sqrt{\mathbf{E}} \mathbf{R}_x \left[\mathbf{I}_6 - \mathbf{A}\mathbf{E}\mathbf{R}_z\mathbf{R}_x \right]^{-1} \mathbf{A}\mathbf{M}_0, \tag{2.10}$$

where all matrices are evaluated at time point TR. The total signal amplitude is calculated according to: $S = |\mathbf{M}|_{xy}^s + |\mathbf{M}|_{xy}^l$. The analytical solution yields the final extended bSSFP signal equation:

$$S \propto \sin(\alpha) \frac{A + B\cos(\alpha)}{C + D\cos(\alpha) + E\cos(2\alpha)}, \tag{2.11}$$

with abbreviations

$$A, B, C, D, E = f(TR, E_{1,2}^{s,l}, k, MWF).$$

A list of the full expressions is given in section 2.7. The limit where only the short pool exists with fraction $MWF = 100\%$ and zero exchange leads to the well-known standard bSSFP equation (eq. 2.1). The equations (2.10) and (2.11) represent the case where relaxation before exchange occurs. Comparison to the case of exchange before relaxation showed negligible signal differences. Therefore, only relaxation before exchange will be considered below.

2.3 Methods

2.3.1 Numerical simulations

All numerical simulations and data analysis were performed using Matlab 2007b (The MathWorks, Inc., Natick, MA, United States). To verify equation (2.11) and to justify the separation of relaxation and exchange processes, numerical simulations of the full set of non-simplified ordinary differential equations (ODE) (eqs. 2.2a-f) were conducted. A standard ODE solver was used to simulate the signal as a function of RF pulse characteristics (flip angle α, RF pulse duration T_{RF}), sequence characteristics (repetition time TR) and two-pool properties (relaxation times, MWF and exchange rate k). Rectangular shaped RF pulses were used for excitation.

To investigate the effects of MT, the modified Bloch equations were extended to 9 dimensions to comprise an additional restricted pool consisting of membranes and macromolecules. Numerical simulations of the 9-dimensional ODE set were performed taking into account saturation of the restricted pool protons, as well as proton exchange with the two free water pools. In general, saturation of the restricted pool protons is achieved by off-resonance irradiation affecting the longitudinal magnetization of the restricted pool and is described by the mean saturation rate [62]:

$$\langle W(\Delta) \rangle = \frac{\pi}{T_{RF}} \int_0^{T_{RF}} \omega_1^2(t) dt \, G(\Delta), \tag{2.12}$$

where Δ is the frequency offset and $G(\Delta)$ the absorption line shape. For the simulations (and measurements) of this work, on-resonance RF pulses were applied, which results in $\Delta \to 0$. The mean saturation rate $W(\Delta \to 0)$ is calculated as a function of the flip angle α and the RF pulse duration T_{RF} according to equation (2.12) and based on a Super-Lorentzian line shape, yielding $G(0) = 1.4 \cdot 10^{-5}$ s^{-1} for a T_2 of the restricted pool of 12 μs [65].

2.3.2   In vivo experiments

Measurements were conducted on a Siemens Avanto 1.5 T system (Siemens Health-care, Erlangen, Germany) in 3D with sagittal orientation based on a 192 x 192 x 144 matrix with 1.3 mm isotropic resolution. The protocol for quantitative *MWF* estimation consisted of:

- A carefully conducted second order manual shim for correction of main mag-netic field inhomogeneities resulting in frequency variations of less than 15 Hz within the shimmed volume containing the whole brain.

- An MPRAGE sequence for anatomical reference and segmentation of WM ($TR/TE = 1760/4.61$ ms, inversion time $TI = 906$ ms, flip angle $\alpha = 7°$, bandwidth = 130 Hz/pixel).

- Multiple bSSFP sequences with 8 varying flip angles $\alpha = 4, 8, 12, ..., 32°$ and non-selective rectangular RF pulses with $T_{RF} = 2$ ms to minimize MT effects (see fig. 2.3b and [66]) ($TR/TE = 5.4/2.7$ ms, bandwidth = 500 Hz/pixel).

- A multi-slice B_1 field map sequence (20 slices, 5 mm slice thickness, 64 x 64 matrix, 4 mm in plane resolution) for the assessment of flip angle deviations based on stimulated echoes resulting from a multi-pulse sequence (α - α - α), analogous to the scheme described in [67].

An acquisition time of 25 min is required to measure the whole protocol (MPRAGE: 3 min, bSSFP: 8 x 2.5 min, B_1 field map: 2 min). In total, six healthy volunteers were investigated. Informed consent was obtained from all participants and exper-iments were approved by local ethics committee.

2.3.3   Postprocessing and data analysis

For image registration and brain extraction, the software packages FSL [68] and AFNI [69] were used. The effective measured B_1 field is depicted as percentage difference from the actual flip angle. According to that, flip angle deviations were calculated pixelwise after B_1 image registration and data interpolation performed with FSL.

The correct assessment of myelin water demands the elimination of possible MT contributions. Therefore, a long RF pulse duration of 2 ms was chosen for the experimental setup of the bSSFP sequence [66]. However, the derivation of the new bSSFP signal equation was based on instantaneously acting RF pulses. Recently, Bieri and Scheffler showed that long pulse durations in bSSFP imaging may lead to a divergence between bSSFP signal prediction and measurement data, making a

finite RF pulse correction necessary [70]. They suggest the following modification to the transverse relaxation T_2 (for non-selective rectangular RF-pulses):

$$T_{2corr} = \left(1 - \xi \frac{T_{RF}}{TR}\right)^{-1} T_2, \;\; with \;\; \xi = 0.68 - 0.125 \left(1 + \frac{T_{RF}}{TR}\right) \frac{T_2}{T_1}, \quad (2.13)$$

where T_{RF} is the duration of the RF pulse. This correction was consistently included in the derived bSSFP signal equation.

One axial, one sagittal and one coronal section per volunteer were selected for analysis. The *MWF* was fitted using the finite RF pulse corrected bSSFP signal equation (eq. 2.11) as fit equation and a nonlinear least squares (NLLS) approach as fit procedure. The fit was performed as a function of the 8 different α. The distance between acquired data and model was minimized with respect to the *MWF* and the signal amplitude. The parameters T_1^s, T_1^l, T_2^s, T_2^l and k were kept constant, whereas TR is known from the measurements (5.4 ms). For the fit of WM regions, a priori values were chosen according to WM literature values: $T_2^s = 10$ ms, $T_2^l = 80$ ms, $T_1^s = 400$ ms, $T_1^l = 900$ ms and $k = 5$ s^{-1} [9, 15–17, 36]. The constant parameters for GM region fitting were fixed analogously according to GM literature values: $T_2^s = 12$ ms, $T_2^l = 90$ ms, $T_1^s = 600$ ms, $T_1^l = 1400$ ms and $k = 5$ s^{-1}.

For the pixelwise fits, a Wiener filter with kernel size 3 was first employed on all images to increase SNR without substantial loss of image details. WM pixels were then segmented based on signal thresholds of the MPRAGE images. The fit of the *MWF* solely was applied to the segmented WM pixels, thereby using the fixed WM parameters given above. Only *MWF* fit results with standard errors $< 100\%$ were allowed.

2.4   Results

2.4.1   Numerical simulations

Figure 2.2 depicts a comparison of the derived bSSFP signal equation (eq. 2.11) with the numerical simulation of the full set of non-simplified ODE (eqs. 2.2a-f). Within the range of experimentally applied flip angles ($4° - 32°$), the extended bSSFP steady state solution clearly underestimates the simulated values by 15% at the maximum difference. This is due to the assumed instantaneously acting RF pulses, which is in contradiction to the long RF pulse duration chosen for experiments to exclude MT effects. The application of a finite RF pulse correction therefore becomes essential. Using the procedure proposed in [70] for the correction of transverse relaxation, finally good agreement ($< 0.1\%$ deviation at $\alpha = 32°$) between the analytical description of the two-pool bSSFP signal and the numerical simulation of the differential equations is achieved. In summary, provided that the

finite RF pulse correction is included, the use of the derived two-pool bSSFP signal equation is valid within the measurement range.
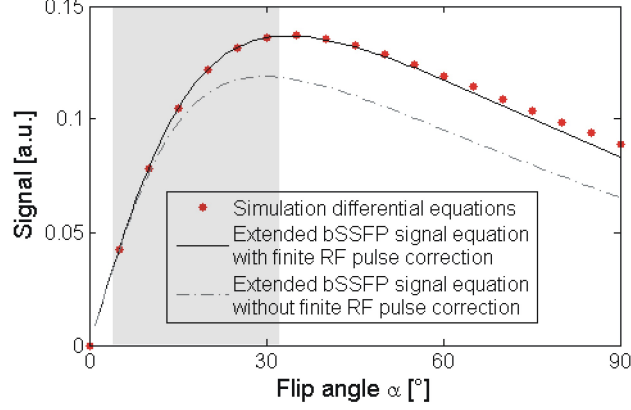

Figure 2.2: *Comparison of the numerical simulation of the differential equations (eqs. 2.2a-f) with the derived extended bSSFP equation using WM parameters: $T_2^s = 10$ ms, $T_2^l = 80$ ms, $T_1^s = 400$ ms, $T_1^l = 900$ ms, $k = 5$ s^{-1}, MWF = 20%, $T_{RF} = 2$ ms, $TR = 2 \cdot TE = 5.4$ ms. The gray dashed line shows the plot of the derived bSSFP signal equation without finite RF pulse correction, the black line illustrates the bSSFP equation including the correction. The total signal is depicted as a function of the flip angle α, the shaded gray area displays the measurement range. Excellent correspondence between the simulation of the differential equations and the finite RF pulse corrected bSSFP signal equation is found in the range of measurements, therefore justifying the application of the finite RF pulse correction.*

Figure 2.3a illustrates further results from the numerical simulations of the two-pool Bloch equations (eqs. 2.2a-f). The signal amplitudes are shown for both pools and for the total signal separately. If exchange processes are taken into account, the short pool will gain signal intensity, which will in return be lost by the long pool. Due to the fast decay of the transverse magnetization of the short pool, less magnetization is available for transfer to the long pool in comparison to the amount exchanged by the long component. The right plot depicts an important difference between the total signal including exchange and the one without exchange: the neglect of proton exchange would lead to an overestimation of the fitted *MWF* of about 10%. In consequence, incorporating proton exchange is necessary to extract the correct *MWF*. Besides that, an obvious difference between the total signal for two pools and the signal for only one existing pool is observed.

Figure 2.3b displays the results from the numerical simulations based on the Bloch equations comprising three pools: the two water pools described above and an additional restricted pool consisting of macromolecules and membranes. The simulations included saturation of the restricted pool, as well as proton exchange between all pools. Two RF pulse durations were investigated: 230 μs (a typical pulse duration used for MT experiments [66]) and 2 ms, as it was applied in our
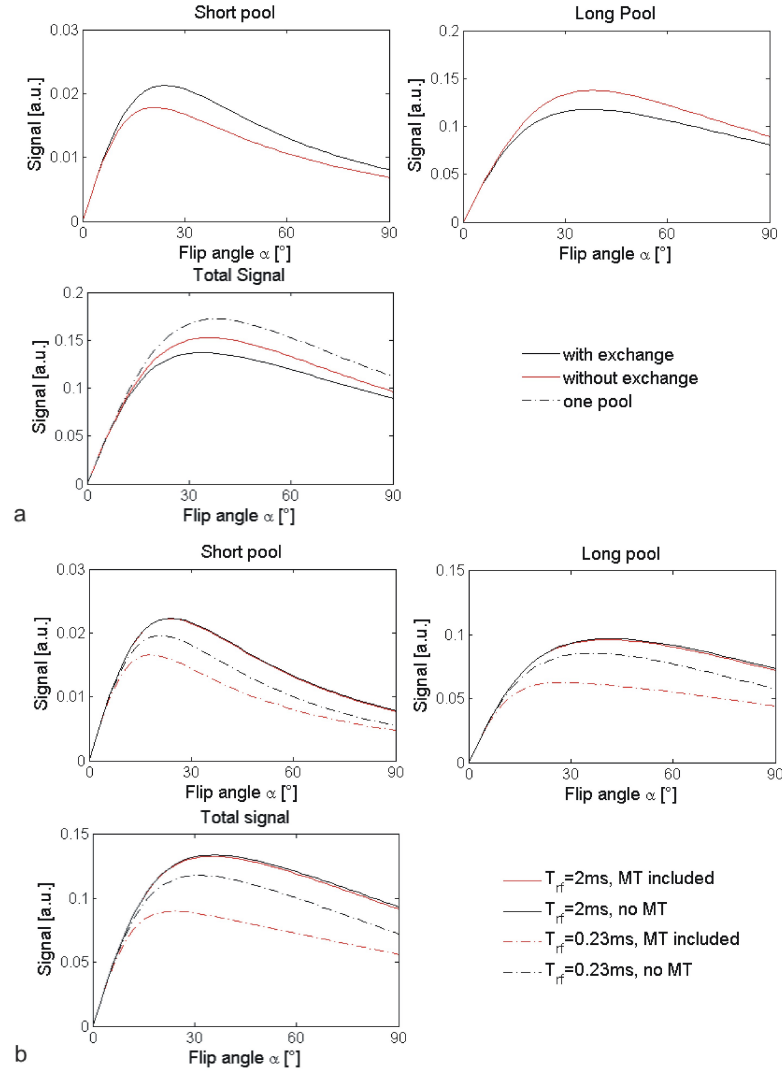
Figure 2.3: *a: Numerical WM bSSFP simulation of the two-pool Bloch equations showing the signal of the short pool, the signal of the long pool and the total signal as a function of the flip angle. Black line: simulation with exchange ($k = 5$ s^{-1}, $MWF = 20\%$), red line: simulation without exchange ($k = 0$ s^{-1}, $MWF = 20\%$) and broken gray line: simulation of one existing pool ($k = 0$ s^{-1}, $MWF = 100\%$). Other parameters used were: $T_2^s = 10$ ms, $T_2^l = 80$ ms, $T_1^s = 400$ ms, $T_1^l = 900$ ms, $T_{RF} = 2$ ms and $TR = 2 \cdot TE = 5.4$ ms. b: Numerical WM bSSFP simulation of the 9-dimensional Bloch equations including an additional third restricted pool (abbreviation r) to investigate the connection between MT and RF-pulse duration. The signal of the short pool, the signal of the long pool and the total signal are illustrated as a function of the flip angle. Parameters used were: $T_2^s = 10$ ms, $T_2^l = 80$ ms, $T_1^s = 400$ ms, $T_1^l = 900$ ms, $MWF = 20\%$, $T_1^r = 1000$ ms, $T_2^r = 12$ μs, $TR = 2 \cdot TE = 5.4$ ms, $k_{sl} = 4$ s^{-1}, $k_{ls} = 1$ s^{-1}, $k_{rs} = 30 \cdot 0.2$ s^{-1}, $k_{sr} = 4.5 \cdot 0.2$ s^{-1}, $k_{rl} = 30 \cdot 0.8$ s^{-1} and $k_{lr} = 4.5 \cdot 0.8$ s^{-1}. Moreover: Fraction of the restricted pool $F_r = 15\%$, therefore $MWF + (1 - MWF) \equiv 85\%$ of the total size of all pools. The signals are plotted with and without MT, based on two RF pulse durations of 2 ms and 230 μs.*

measurements. For $T_{RF} = 230$ μs, an evident signal difference between MT and no MT is observed, which represents the background of measuring MT effects. On the other hand, the correct assessment of the *MWF* demands the elimination of possible MT contributions. This can be achieved by choosing an RF pulse duration of 2 ms. Due to the decrease in RF pulse bandwidth, the signal difference between MT and no MT becomes negligible small for 2 ms duration. Therefore, MT effects can definitely be excluded from the experiments performed in this study.

2.4.2   In vivo experiments

Quantitative *MWF* evaluation is exemplarily illustrated in figure 2.4a. The bSSFP signal intensities from two WM and two GM regions from one healthy subject are fitted based on equation (2.11) applying either the constant WM or GM parameters. Resulting *MWF* values are given in table 2.1, together with the sum of squares of the residuals (SSQ). The fitted *MWF* of the GM regions are considerably smaller than the *MWF* obtained from WM regions yielding good correspondence with literature values [9, 13, 16, 17, 19, 21, 22, 30, 31, 36, 45, 71]. WM and GM results from single-pool fitting using the finite RF pulse corrected conventional bSSFP equation (2.1) are presented in figure 2.4b. For the single-pool fit, the distance between acquired data and equation (2.1) was minimized with respect to the transverse relaxation T_2 and the signal amplitude, while leaving T_1 fixed (850 ms for WM, 1200 ms for GM). Due to the dependence on the ratio T_2/T_1 of the conventional bSSFP formula (eq. 2.1) [46], fitting of both relaxation times was not feasible. The resulting single-pool T_2 values are shown in table 2.1, together with the SSQs. In general, both fit procedures yield small residuals of less than 2%. To evaluate the significance, direct comparison of the different SSQs is valid, because both the two-pool and the single-pool fit procedure possess 6 degrees of freedom (8 data points - 2 unknowns). Since the SSQs from the two-pool bSSFP fitting are in each region reduced compared to the singe-pool fitting SSQs, one can conclude that the extended two-pool bSSFP equation yields significantly better fit results than the application of the conventional bSSFP formula.

Axial, sagittal and coronal quantitative myelin water maps with an isotropic resolution of 1.3 mm are presented in figure 2.5 for WM of five normal appearing human brains. Mean *MWF* values from segmented WM pixels with corresponding standard deviations are listed in table 2.2, separately indicated for the investigated subjects. Besides some small problems with off-resonance artifacts affecting particularly the regions near the nasal cavities, the derived *MWF* maps appear smooth and high correlation between individual subjects is observed. Furthermore, the mean *MWF* values correspond to literature values [9, 13, 16, 17, 19, 21, 22, 30, 31, 36, 45, 71].
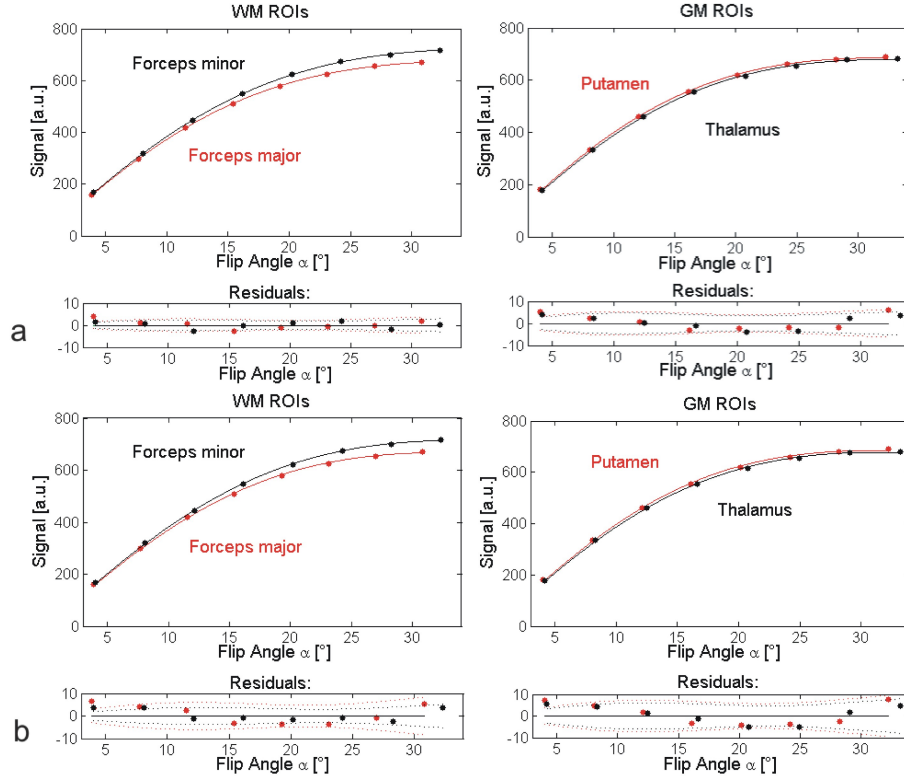
Figure 2.4: ***a:*** *Introductory examples to the two-pool bSSFP analysis showing MWF parameter fitting of two WM and two GM ROIs from one healthy subject. NLLS fit procedure and application of the finite RF pulse corrected extended bSSFP signal equation (eq. 2.11) with either constant WM parameters $T_2^s = 10$ ms, $T_2^l = 80$ ms, $T_1^s = 400$ ms, $T_1^l = 900$ ms and $k = 5$ s^{-1} or constant GM parameters $T_2^s = 12$ ms, $T_2^l = 90$ ms, $T_1^s = 600$ ms, $T_1^l = 1400$ ms and $k = 5$ s^{-1} yield MWF results displayed in table 2.1. **b:** Single-pool fitting examples of the regions from figure 2.4a. NLLS fit procedure and application of the finite RF pulse corrected conventional bSSFP formula (eq. 2.1) with either the constant WM parameter $T_1 = 850$ ms or the constant GM parameter $T_1 = 1200$ ms lead to single-pool T_2 fit results given in table 2.1. Moreover, fitting residuals and 95% confidence intervals are presented. Sum of squares of the fitting residuals are listed in table 2.1.*

Table 2.1: *ROI results derived from two-pool bSSFP model fitting (eq. 2.11) and single-pool fitting using the conventional bSSFP equation (eq. 2.1) (ROI results ± standard error).*

	WM		GM	
	Forceps minor	Forceps major	Putamen	Thalamus
Two-pool fitting[a]				
MWF [%]	15.4 ± 1.5	11.1 ± 1.0	5.8 ± 2.0	3.9 ± 1.6
SSQ[b]	29.7	18.6	92.9	68.1
Single-pool fitting[c]				
T_2 [ms]	53.6 ± 3.2	58.7 ± 2.0	67.7 ± 4.2	70.7 ± 3.6
SSQ[b]	130.5	51.3	187.8	128.5

[a]Fixed WM parameters: $T_2^s = 10$ ms, $T_2^l = 80$ ms, $T_1^s = 400$ ms, $T_1^l = 900$ ms and $k = 5$ s^{-1}; fixed GM parameters: $T_2^s = 12$ ms, $T_2^l = 90$ ms, $T_1^s = 600$ ms, $T_1^l = 1400$ ms and $k = 5$ s^{-1}.
[b]Sum of squares of the fit residuals.
[c]Fixed WM parameter: $T_1 = 850$ ms; fixed GM parameter: $T_1 = 1200$ ms.

Table 2.2: *MWF [%] derived from pixelwise two-pool bSSFP model fitting of segmented white matter (pixelwise mean ± pixelwise SD). Corresponding MWF parameter maps are illustrated in figure 2.5.*

	Subject 1	Subject 2	Subject 3	Subject 4	Subject 5
Axial view	11.2 ± 4.0	13.6 ± 5.1	14.8 ± 6.1	12.5 ± 4.9	11.9 ± 4.6
Sagittal view	12.3 ± 3.8	13.1 ± 4.5	14.8 ± 5.0	12.2 ± 3.7	11.4 ± 3.8
Coronal view	11.9 ± 3.3	12.3 ± 4.0	14.2 ± 4.7	13.2 ± 4.4	13.2 ± 4.2

Figure 2.5: *Axial, sagittal and coronal sample images from five healthy volunteers showing 1.3 mm isotropic high-resolution MWF parameter estimates as derived from two-pool bSSFP model fitting using the NLLS algorithm and the extended bSSFP fit equation (eq. 2.11). Analysis was solely applied to segmented WM pixels using the constant WM parameters $T_2^s = 10$ ms, $T_2^l = 80$ ms, $T_1^s = 400$ ms, $T_1^l = 900$ ms and $k = 5$ s^{-1}. Mean values with corresponding standard deviations are listed in Table 2.2.*

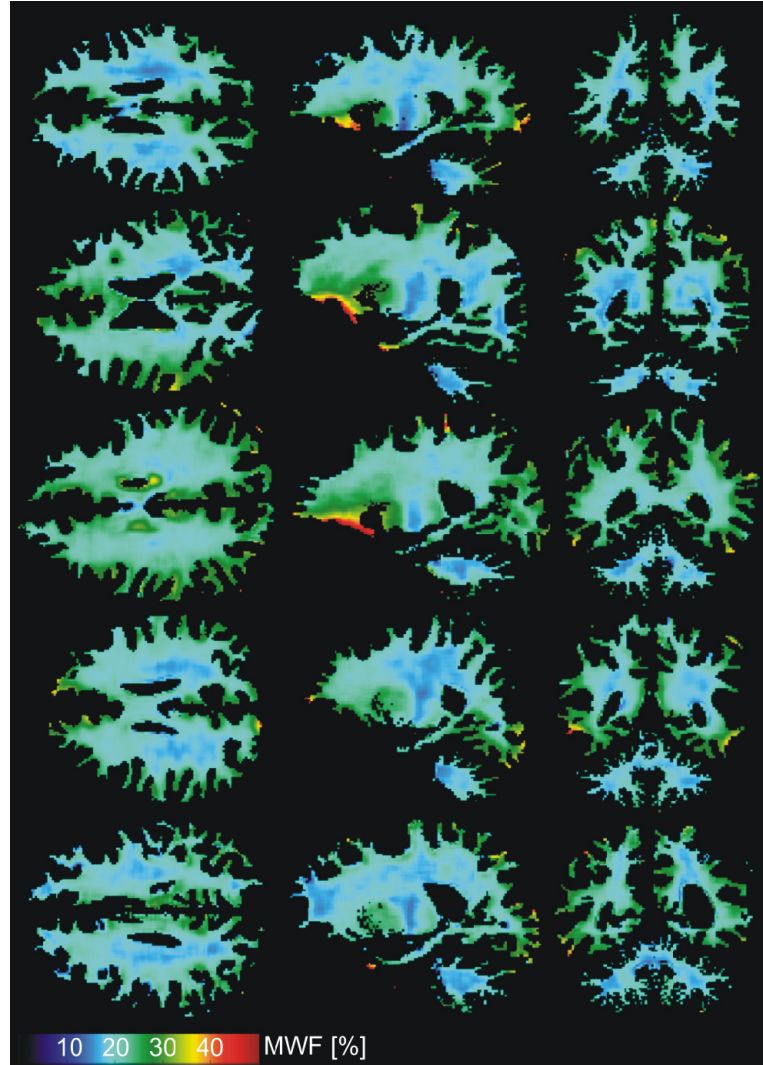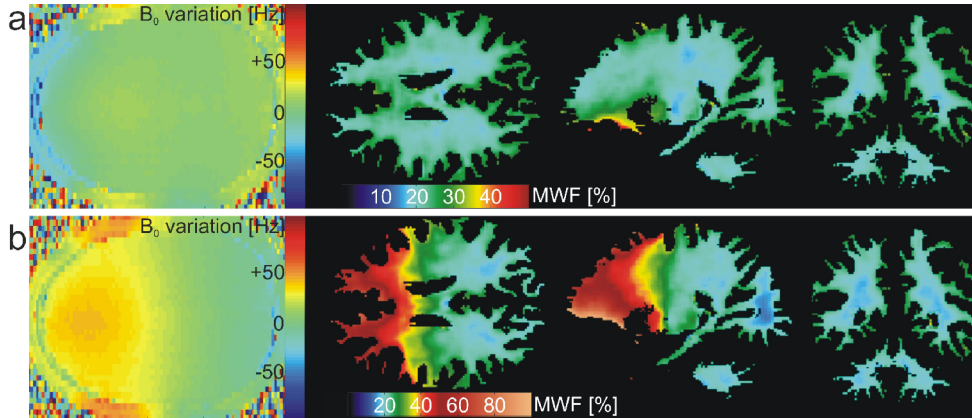**Figure 2.6:** ***Right:*** *Axial, sagittal and coronal sample images of a sixth healthy volunteer showing 1.3 mm isotropic high-resolution MWF parameter estimates as derived from two-pool bSSFP model fitting using the NLLS algorithm and the extended bSSFP fit equation (eq. 2.11).* ***Left:*** *Axial quantitative B_0 maps having the same location as the axial sample image shown on the right side. Maps were computed based on two gradient recalled echo images with different echo times.* ***a:*** *Regular measurement protocol (as described in section 2.3).* ***b:*** *Manually induced increase of the B_0 inhomogeneity by 10 $\mu T/m$ (in y-direction from frontal to posterior) results in frequency variations of about 40 Hz in the B_0 map and leads to the formation of an apparent MWF gradient reaching from frontal to posterior WM having the size of $\sim$ 60%.*

To investigate the influence of B_0 inhomogeneities on the experimental bSSFP data, the measurement protocol of the sixth healthy volunteer was expanded. In addition to the regular protocol described in section 2.3, a standard Siemens protocol based on two gradient recalled echo sequences with different *TE* was measured to calculate quantitative B_0 maps. The field mapping sequence had sagittal orientation and consisted of a 128 x 128 matrix with 2 x 2 mm^2 resolution and 36 slices with 4 mm slice thickness. *TR* was 455 ms, $TE_1 = 4.76$ ms, $TE_2 = 9.52$ ms, $\alpha = 60°$ and bandwidth = 260 Hz/pixel. Figure 2.6a illustrates the axial, sagittal and coronal sample images showing 1.3 mm isotropic high-resolution *MWF* parameter estimates and on the left side one quantitative B_0 map having the same location as the axial *MWF* map. Figure 2.6b depicts the second part of the measurement, where the 8 bSSFP sequences were repeated with a manual increase of the B_0 inhomogeneity by 10 μT/m (in y-direction from frontal to posterior). This modification leads to frequency variations of about 40 Hz in the B_0 map and results in the formation of an apparent *MWF* gradient reaching from frontal to posterior WM. Therefore, it can be concluded that the fit procedure introduced in this work reveals to be highly sensitive to B_0 variations arising i.e. from dental fillings. For that reason, a carefully conducted high order manual shim is essential for obtaining smooth *MWF* parameter maps.

2.5   Discussion

In this work, a new bSSFP signal equation based on a two pool water exchange model was derived that was used as fit equation for the quantitative analysis of bSSFP measurement data with varying flip angles. The distance between acquired data and model was minimized with respect to the *MWF* and the signal amplitude, while keeping the parameters T_1^s, T_1^l, T_2^s, T_2^l and k fixed. Obtained results (tables 2.1 and 2.2) correspond to previously reported literature values [9, 13, 16, 17, 19, 21, 22, 30, 31, 36, 45, 71]. Moreover, the *MWF* parameter results from GM regions are considerably smaller than the *MWF* obtained from WM regions yielding as well agreement with literature. Aside from that, T_1 of myelin water was assumed to be considerably shorter than the longitudinal relaxation of the intra- and extracellular water of the axon. Omitting this difference would lead to a serious overestimation of the *MWF* of about 10% and therefore result in *MWF* values inside the upper range of literature values.

On-resonance MT effects were excluded from experiments by choosing long RF pulse durations (fig. 2.3b). However, the selection of long RF pulse durations requires the use of a finite pulse correction (fig. 2.2), which was applied to the derived bSSFP signal equation. Another important error source is B_1 field inhomogeneity leading to flip angle deviations of maximal 10% in the experimental data. To eliminate these systematic errors, the applied flip angles were corrected prior to data analysis, by performing B_1 field mapping. Furthermore, problems with B_0 inhomogeneities were avoided by carefully conducting high order manual shims. The neglect of manual shimming leads to the formation of high *MWF* gradients in the parameter maps making this sort of correction essential (fig. 2.6b). Issues with B_0 inhomogeneities would as well play an important role in case of switching to higher magnetic field strengths. There, not only problems with *MWF* gradients would arise, but one would also have to deal with formation of bSSFP off-resonance bands in the acquired images. Nonetheless, by applying careful manual shimming and RF phase cycling to avoid banding artifacts, measurements at higher field strengths may be feasible. Increased imaging time due to the phase cycling approach might be reduced by parallel imaging techniques.

The proposed two-pool analysis procedure is based on fitting the *MWF* and the signal amplitude and fixing the parameters T_1^s, T_1^l, T_2^s, T_2^l and k. In principle, the choice to fix certain parameters was made based on two reasons. First, the derived bSSFP signal equation is extremely complex making it impossible to fit all parameters, especially in presence of the simple bSSFP curve behavior. Secondly, there are four unknown relaxation times present in the two-pool model, which can not be measured directly with other techniques and then inserted backwards into the model. In particular, the knowledge about the two longitudinal relaxation times is very limited from literature.

However, it is clear from previous work that the relaxation times show spatial and pathological variation and are not globally constant. To investigate the stability of the MWF parameter, variation of the fixed parameters was performed, which is shown in figure 2.7 for one WM region. Thereby, each of the constant parameters was varied between $\pm$ 10%. Variation of the exchange rate results in extremely small deviation of the fitted MWF ($< \pm$ 4%) (fig. 2.7a). The discrepancy of the MWF values upon variation of T_2^s and T_1^s is as well in a reasonable range ($< \pm$ 10%) (fig. 2.7b,c). On the other hand, the alteration of the fitted MWF caused by variation of T_2^l and T_1^l is more severe. However, the smoothness of the derived MWF parameter maps (fig. 2.5) indicates that the real spatial WM parameter variation of the investigated healthy subjects must be smaller than $\pm$ 10%, because the standard deviations of our MWF results are broadly comparable to literature results [9, 13, 16, 17, 19, 21, 22, 30, 31, 36, 45, 71]. Nevertheless, the strong dependence of the MWF on T_2^l and T_1^l demonstrates that the applicability of the proposed method not only to pathologies, but also to maturation or ageing of WM is considerably impaired.

Only recently, Deoni et al. introduced a similar approach to myelin water imaging, but used, in contrary to our study, a complex hybrid approach consisting of a genetic algorithm and a local search method to fit all unknown parameters [13]. In their work, presented MWF results from WM pixels of healthy subjects lie inside the upper range of literature values (averaged $MWF = 29.5 \pm 5.3\%$) and are considerably higher than the results presented here. Presumably, the observed difference arises not only due to the fixed parameters in this study, but also due to the negligence of B_1 inhomogeneities and MT effects in the work of Deoni et al..

Lately, some groups predicted the two-pool model to be inappropriate and supposed instead a three pool model including the axonal water as separate pool (fractional pool size $\sim$ 50%), the myelin water ($\sim$ 20%) and the extracellular water as third pool ($\sim$ 30%) [21, 58, 59]. According to these studies, a significant amount of signal from the axonal water could be misclassified into the myelin water signal if only two pools were considered. This, in turn, would lead to an eventual global overestimation of the fitted MWF.

Figure 2.8 illustrates fit results from WM regions showing on the one hand the incorporation of all 8 flip angles to data analysis and on the other hand the reduction to either 3 or 4 flip angles. Application of 4 different flip angles results in similar values for the MWF and slightly enhanced standard errors, whereas the decrease to 3 flip angles is impractical due to extreme high standard errors ($> 100\%$). The reduction to 4 flip angles would lead to a considerable shortening of acquisition time from 25 min to 15 min.

The technique presented in this work offers a stable approach to high-resolution 3D myelin water imaging of WM from healthy subjects. However, the application of the proposed technique is limited due to the fixed parameters included in the analysis
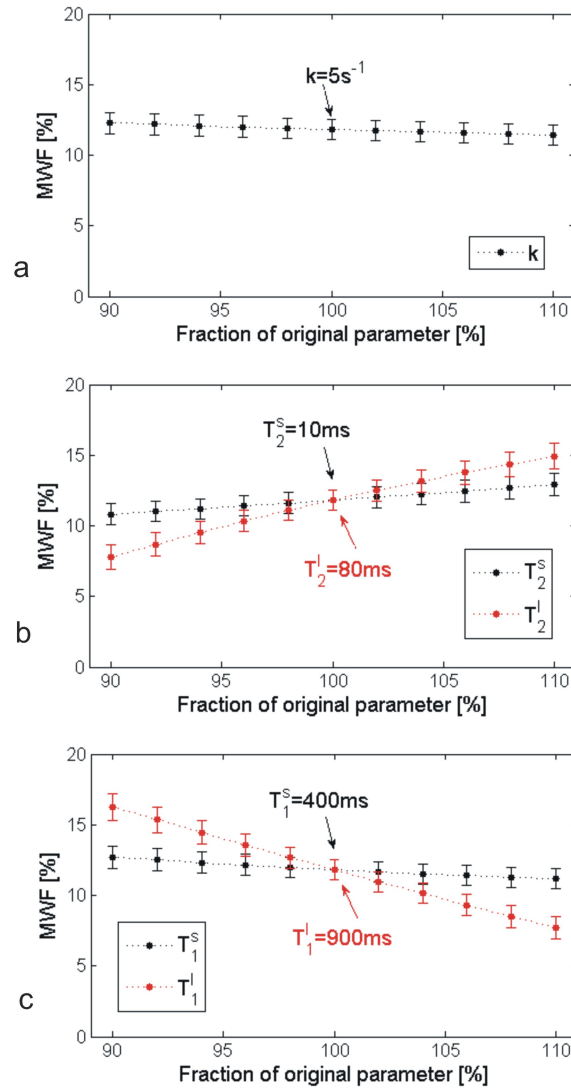
Figure 2.7: *Estimation of MWF stability upon variation ($\pm$ 10%) of constant fit parameters for one WM region. MWF fit results $\pm$ standard errors are given as a function of the parameter variation. In each case, one parameter is varied while leaving the remaining parameters unmodified. **a:** Variation of the exchange rate k. **b:** Variation of the transverse relaxation times T_2^s and T_2^l. **c:** Variation of the longitudinal relaxation components T_1^s and T_1^l.*

Figure 2.8: *Fit results of two WM regions evaluated in all healthy subjects showing on the one hand the incorporation of all 8 flip angles to the fit with $\alpha = 4,8, ...,32°$ and on the other hand the reduction to 4 flip angles with $\alpha = 4, 16, 24, 32°$. The proposed flip angle decrease results in similar values for the MWF and slightly enhanced standard errors, which may lead to a possible shortening of measurement time from 25 to 15 minutes. Due to the extreme high standard errors, the reduction to 3 flip angles is impractical.*
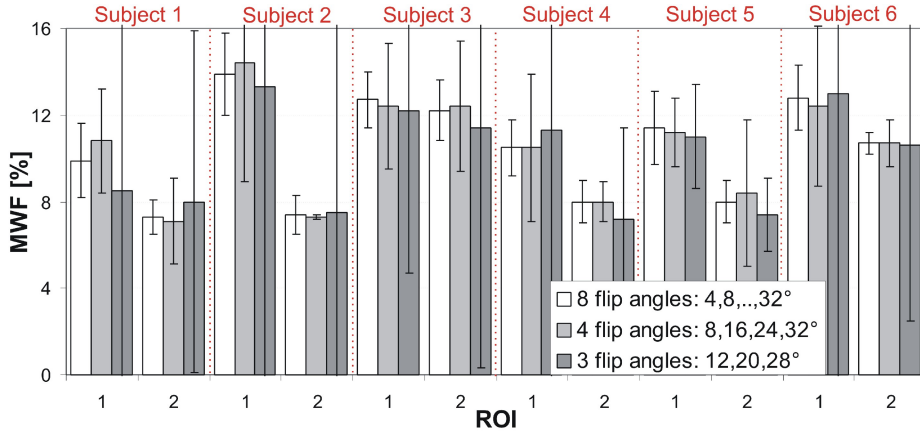
procedure. Nevertheless, this study provides a non-negligible contribution to the relatively new field of 3D myelin water quantification with whole-brain coverage.

2.6   Conclusion

In this work, a new bSSFP signal equation based on a two-pool water exchange model was derived to quantify the MWF of WM from healthy subjects. In the course of the proposed two-pool model analysis, the MWF and the signal amplitude were fitted as single unknowns, while a priori assumptions were made for the other parameters of the two-pool system. The influence of B_0 and B_1 inhomogeneities, as well as MT effects and the requirement for a finite RF pulse correction were discussed. Moreover, the stability of the derived MWF values upon variation of the fixed parameters was investigated. MWF values found in this study showed good correspondence with literature. However, the strong dependence of the MWF on the fixed two-pool parameters considerably impairs the clinical application of the proposed technique.

2.7   Appendix

The extended bSSFP signal equation is written as:

$$S = \sin(\alpha)\frac{A + B\cos(\alpha)}{C + D\cos(\alpha) + E\cos(2\alpha)},$$

with full abbreviations given by:

$$
\begin{aligned}
A = &\ e^{2kTR}\left(1 + E_1^l(MWF - 1) - E_1^s MWF\right)\left(\sqrt{E_2^l}(MWF - 1) - \sqrt{E_2^s}MWF\right)\\
&- e^{kTR}(E_1^s - E_1^l)\left(\sqrt{E_2^s} + (E_2^s - 1)\sqrt{E_2^l} - \sqrt{E_2^s}E_2^l\right)(MWF - 1)MWF\\
&+ \sqrt{E_2^s}\sqrt{E_2^l}\left(\sqrt{E_2^s}(MWF - 1) - \sqrt{E_2^l}MWF\right)\ldots\\
&\times \left(-E_1^l MWF + E_1^s(-1 + E_1^l + MWF)\right),\\
B = &\ e^{kTR}\Bigg[(1 - E_1^l)(E_1^s - E_2^s)\sqrt{E_2^l}\ldots\\
&+ \left((1 - E_1^s)E_1^l\sqrt{E_2^s} + (E_1^l - 1)(E_1^s - E_2^s)\sqrt{E_2^l} + (E_1^s - 1)\sqrt{E_2^s}E_2^l\right)MWF\Bigg],\\
C = &\ e^{2kTR}\Bigg[-1 + \left(E_1^l(MWF - 1) - E_1^s MWF\right)\left(E_2^l(MWF - 1) - E_2^s MWF\right)\Bigg]\\
&+ \frac{1}{2}e^{kTR}\Bigg[-(E_1^s - E_2^s)(E_1^l - E_2^l) + 4(E_1^s - E_1^l)(E_2^s - E_2^l)MWF\ldots\\
&- 4(E_1^s - E_1^l)(E_2^s - E_2^l)MWF^2\Bigg]\\
&+ E_1^l MWF\left(E_2^s(1 - MWF) + E_2^l MWF\right)\\
&+ E_1^s\left(E_2^s\left(-E_1^l E_2^l + (MWF - 1)^2\right) - E_2^l(MWF - 1)MWF\right),\\
D = &\ e^{2kTR}\Bigg[E_1^l - E_2^l + (E_1^s - E_1^l - E_2^s + E_2^l)MWF\Bigg]\\
&- e^{kTR}\Bigg[(E_1^s - E_2^s)(-1 + E_1^l E_2^l)\ldots\\
&+ \left(-E_1^l - E_2^s + E_2^l + E_1^l E_2^s E_2^l + E_1^s\left(1 + E_1^l E_2^s - (E_1^l + E_2^s)E_2^l\right)\right)MWF\Bigg]\\
&+ E_1^l E_2^s E_2^l MWF - E_1^s\left(E_2^s E_2^l(MWF - 1) + E_1^l(E_2^s - E_2^s MWF + E_2^l MWF)\right),\\
E = &\ -\frac{1}{2}e^{kTR}(E_1^s - E_2^s)(E_1^l - E_2^l).
\end{aligned}
$$

Chapter 3

Myelin water imaging using 3D mGRE pulse sequences

3.1   Introduction

Only recently, a new approach to myelin water imaging using 2D multi-gradient-echo pulse sequences was introduced by Du et al. [21] and is based on the idea that not only T_2 decay of brain tissue is multi-exponential, but also T_2^* relaxation. In the work of Du et al., acquisition of T_2^* decay was performed in postmortem brains at 3 T and analyzed by using a fixed three-pool WM model that benefits from additional fitting of the myelinated axon water pool and can therefore give insight into the axonal integrity. The proposed method was later on successfully extended to in vivo measurements of healthy subjects [60]. *MWF* mapping based on mGRE pulse sequences has the important advantages of a short first echo time and short echo spacing, which enable accurate sampling of the fast myelin water signal decay. Moreover, the application of mGRE sequences allows fast multi-slice data acquisitions (5 slices with 126 different echoes in less than 9 min. [21]).

However, the procedure presented by Du and his group suffers from a lack of volume coverage and does not offer whole brain coverage due to the 2D acquisition scheme [21]. In this chapter, a new solution to 3D in vivo myelin water imaging is presented, which uses mGRE pulse sequences at 1.5 T for data acquisition and non-negative least squares algorithms for analysis of the multi-component T_2^* relaxation. Quantitative myelin water maps are generated based on analysis of the derived T_2^* spectra. *MWF* results from measurements of healthy subjects and as well MS patients are illustrated. The proposed technique offers not only whole brain coverage, but also a clinically feasible scan time of less than 10 minutes for the acquisition of 96 different echo times. Moreover, the influence of B_0 inhomogeneities on the derived myelin water maps and other effects that can possibly alter the obtained *MWF* values are discussed in this chapter.

3.2   Methods

3.2.1   Experimental setup

Measurements were conducted on 3 healthy volunteers and 8 confirmed MS patients using a whole body 1.5 T MRI system (Magnetom Avanto, Siemens Healthcare, Erlangen, Germany) and a 12-channel phased-array head coil. Informed consent was obtained from all participants and experiments were approved by local ethics committee. The protocol consisted of:

  - A carefully conducted second-order manual shim for correction of main magnetic field inhomogeneities resulting in frequency variations of less than 15 Hz within the shimmed volume containing the whole brain.

- A 3D T_2^* weighted mGRE pulse sequence based on a sagittal matrix of 99 x 110 x 88, 2.2 x 2 x 2 mm^3 resolution and 96 different echo times with a first echo time of 1.4 ms and an echo spacing of 0.99 ms. The sequence had alternating readout gradient polarities, RF spoiling and the phase-encoding gradients were rewound at the end of each echo train. Sinc-shaped slice-selective pulses with duration of 700 μs were used for excitation. To optimize the sensitivity and thus the signal-to-noise ratio of the experiment, TR was set to $1.3 \cdot T_2^*$ (long component) $\approx 1.3 \cdot 75$ ms = 98 ms [72]. The given TR was then consequently filled with echoes having the minimal echo spacing, finally resulting in the 96 different echo times mentioned above ($TE_{96} = 95.5$ ms). Gradient spoiling of 2π across a voxel was applied at the end of TR to eliminate possible remaining transverse magnetization. Moreover, the flip angle was chosen to be 32° (in accordance to the Ernst angle of WM), the readout bandwidth was 1300 Hz/pixel, no averaging was performed and partial Fourier was used collecting 6/8 of k-space. Total scan time of the mGRE sequence was 9 min. 40 sec. To validate the quality of the manual shimming procedure, the phase images of the mGRE sequence were reconstructed in addition to the magnitude data.

- A clinical routine 3D MPRAGE sequence for anatomical reference based on a sagittal matrix of 240 x 256 x 160 and 1 mm isotropic resolution with $TR/TE = 2080/3$ ms, inversion time $TI = 1100$ ms, flip angle $\alpha = 15°$ and bandwidth = 130 Hz/pixel.

- An additional clinical routine turbo spin-echo sequence based on 40 axial slices with slice thickness 3 mm, image matrix 192 x 256 and 1 x 1 mm^2 in-plane resolution. The sequence had proton density (PD) weighted and T_2 weighted contrasts for lesion localization in MS patients. Scan parameters were $TE_1 = 9.3$ ms, $TE_2 = 112$ ms, $TR = 3980$ ms, echo train length = 7 and bandwidth = 195 Hz/pixel.

In order to test the influences of B_0 inhomogeneities and T_1 weighting on the measurement protocol and the myelin water results, one healthy subject was repeatedly scanned. The first acquisition consisted of the normal protocol described above. The second scan was performed with a manually induced increase of the B_0 inhomogeneity by 10 μT/m in z-direction (no other modifications of the experimental setup took place). Additionally, a third measurement was conducted at a very low flip angle of 10° (other parameters remained unaltered), where the mGRE signal approximately is independent of potential T_1 effects.

3.2.2   Postprocessing and data analysis

For brain extraction of all data sets and registration of the structural MPRAGE, PD weighted and T_2 weighted data sets with reference to the first contrast of the

mGRE sequence, the software packages FSL [68] and AFNI [69] were used. The T_2^* weighted data used for MWF quantification were not registered, but a median filter with kernel size 3 was applied before fitting [73]. Data analysis was performed using Matlab 2007b (The MathWorks, Inc., Natick, MA, United States).

For analysis and fitting of the acquired mGRE data, the signal amplitudes y_i of the T_2^* decay were assumed to be of multi-exponential behavior:

$$y_i = \sum_{k=1}^{M} s_k exp(-t_i/T_{2k}^*), \ i = 1, 2, ..., N, \tag{3.1}$$

where t_i are the $N = 96$ measured echo times, T_{2k}^* are $M = 120$ logarithmically spaced T_2^* relaxation times in the range of $1.5 \cdot TE_1 = 2.1$ ms and 300 ms and s_k is the relative amplitude for each corresponding T_2^* relaxation time. The expression from equation (3.2) was then minimized by using a conventional NNLS algorithm and applying the energy constraint given in equation (3.3), finally resulting in regularized smooth T_2^* distributions [40, 41].

$$\chi^2 + \mu \sum_{k=1}^{M} s_k^2, \ \mu \geq 0, \tag{3.2}$$

$$1.02\chi_{min}^2 \leq \chi^2 \leq 1.025\chi_{min}^2. \tag{3.3}$$

In general, the larger the μ parameter, the smoother the T_2^* distribution becomes at the cost of misfit. The case of $\mu = 0$ however would result in a T_2^* distribution consisting of discrete peaks. The applied regularization has the crucial advantages of delivering more consistent fits in the presence of noise and resulting in distributions that better reflect the underlying structure of biological tissues [40, 41]. The MWF finally could be calculated according to:

$$MWF[\%] = \frac{\sum s_k(T_2^* < 25ms)}{\sum s_k} \cdot 100. \tag{3.4}$$

Applying NNLS algorithms is the most frequently used fitting procedure in literature for quantitative myelin water determination based on conventional multi-spin-echo sequences [9, 19, 22, 36, 41, 45, 71]. It requires no a-priori knowledge about the number of existing components and represents therefore an unbiased technique of analyzing multi-exponential data. Because of its previous successful application for analysis of T_2 decay, the NNLS method was incorporated in this study to analyze the acquired T_2^* relaxation and calculate the MWF based on the T_2^* distribution.

In order to validate the quality of the manual shimming procedure, B_0 maps were calculated from the mGRE data sets. Based on the complex information of the 2nd (2.4 ms) and the 6th (6.4 ms) echo and with the help of the four-quadrant arctangent function, the phase differences and hence the B_0 variation was determined [74].

3.3   Results

3.3.1   Healthy subject results

Figure 3.1a shows exemplary acquired mGRE images of one healthy subject. The illustrated time series represents images acquired at echo numbers 1, 32, 64 and 96. The SNR of the image acquired at TE_1 yields 140 (calculation was based on the mean value of a small homogeneous WM ROI divided by the standard deviation of a large background ROI). This result indicates a low level of spatial noise in the mGRE data set and eliminates therefore possible inaccuracies with the application of the NNLS algorithm [42, 75]. The corresponding quantitative B_0 maps are depicted in figure 3.1b revealing small variations of less than 5 Hz inside the brain. In addition, effects from natural sources of poor shim like the nasal sinus or the auditory canal could be reduced to a minimum and prove the high quality of the manual shimming procedure.

Exemplary fit results of single pixels from one healthy subject are depicted in figure 3.2 (a: WM pixel, b: GM pixel). Both pixels present excellent correspondence between measured data points and fitted signals yielding residuals $< 5\%$. The corresponding regularized T_2^* distribution of the WM pixel depicts two isolated smooth peaks, the first one belonging to the myelin water pool, whereas the second peak can be assigned to the intra- and extracellular water present in brain tissue ($MWF = 6.2\%$). In contrast to figure 3.2a, the fitting procedure solely detects one water pool for the GM pixel resulting in a T_2^* distribution with one peak and $MWF = 0\%$.

MWF maps of one healthy volunteer are illustrated in figure 3.3. The derived MWF parameter maps look smooth in all three spatial directions and no severe off-resonance artifacts (for example near the nasal cavities) are present. Due to the overall low MWF pixelwise results, the applied fit procedure is mainly conducted in WM pixels, whereas $MWF = 0\%$ is observed in GM pixels (in correspondence to the examples from above). However, one might detect partial volume effects in the MWF maps having consequent lower MWF values than surrounding pure WM pixels.

The influence of static magnetic field inhomogeneities on the proposed measurement protocol is presented in figure 3.4. The manually induced small B_0 gradient leads to a non-exponential signal modulation that results in a relative signal increase at the late echoes (fig. 3.4b). In turn, the relative overemphasis of the late echoes artificially modifies the curve slope and finally results in an overestimation of the MWF (fig. 3.4c). A loss of WM contrast in the resulting MWF maps can be observed in addition. These results exactly correspond to the findings of Hwang et al. [60] and demonstrate the importance of the second-order manual shim in order to reduce B_0 inhomogeneities and achieve accurate MWF values.
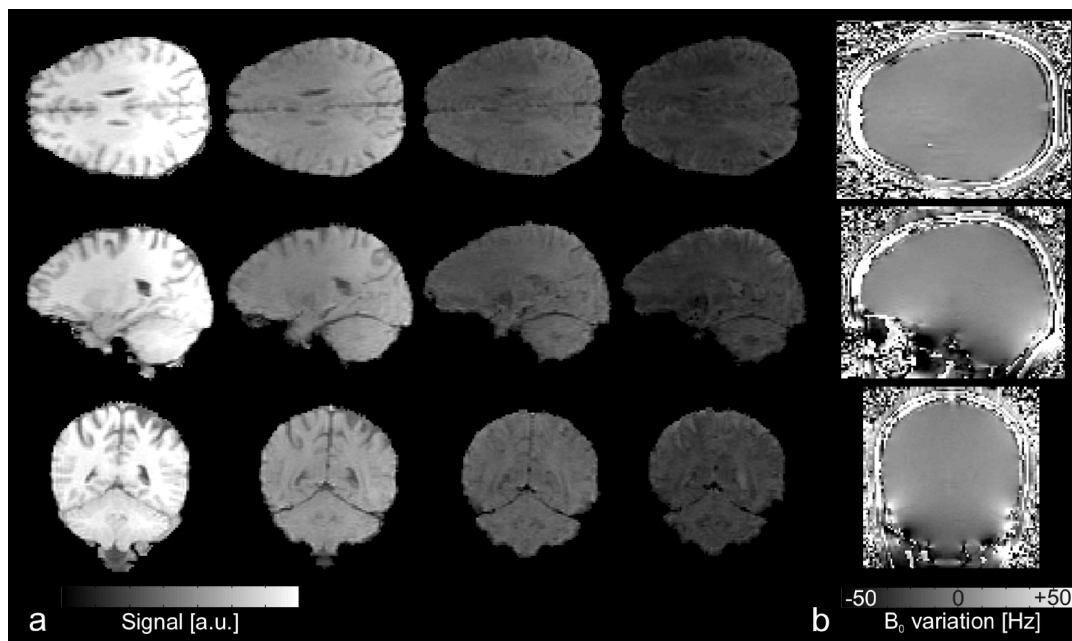
Figure 3.1: *a:* *Exemplary axial, sagittal and coronal mGRE images of one healthy subject representing echoes number 1, 32, 64 and 96 with corresponding echo times of 1.4, 32.1, 63.8 and 95.5 ms. **b: Quantitative B_0 maps (given in Hz off-resonance) having the same location as the images shown on the left side. B_0 was computed based on the complex data of echo 2 (2.4 ms) and echo 6 (6.4 ms) of the mGRE series. A variation of less than 5 Hz was found inside the brain proving the high quality of the conducted second order manual shim. Moreover, effects from natural sources of magnetic field inhomogeneities like the nasal sinus or the auditory canal could effectively be reduced.*

Figure 3.2: *Introductory fit examples of two pixels from one healthy subject.* **Top:** *Acquired T_2^* decay curve (red crosses) and fitted signal using NNLS algorithm (black line).* **Center:** *Corresponding regularized T_2^* distribution.* **Bottom:** *Fit residuals.* **a:** *WM pixel, location illustrated in figure 3.3a in red.* **b:** *Gray matter pixel, location shown in figure 3.3a in yellow.*
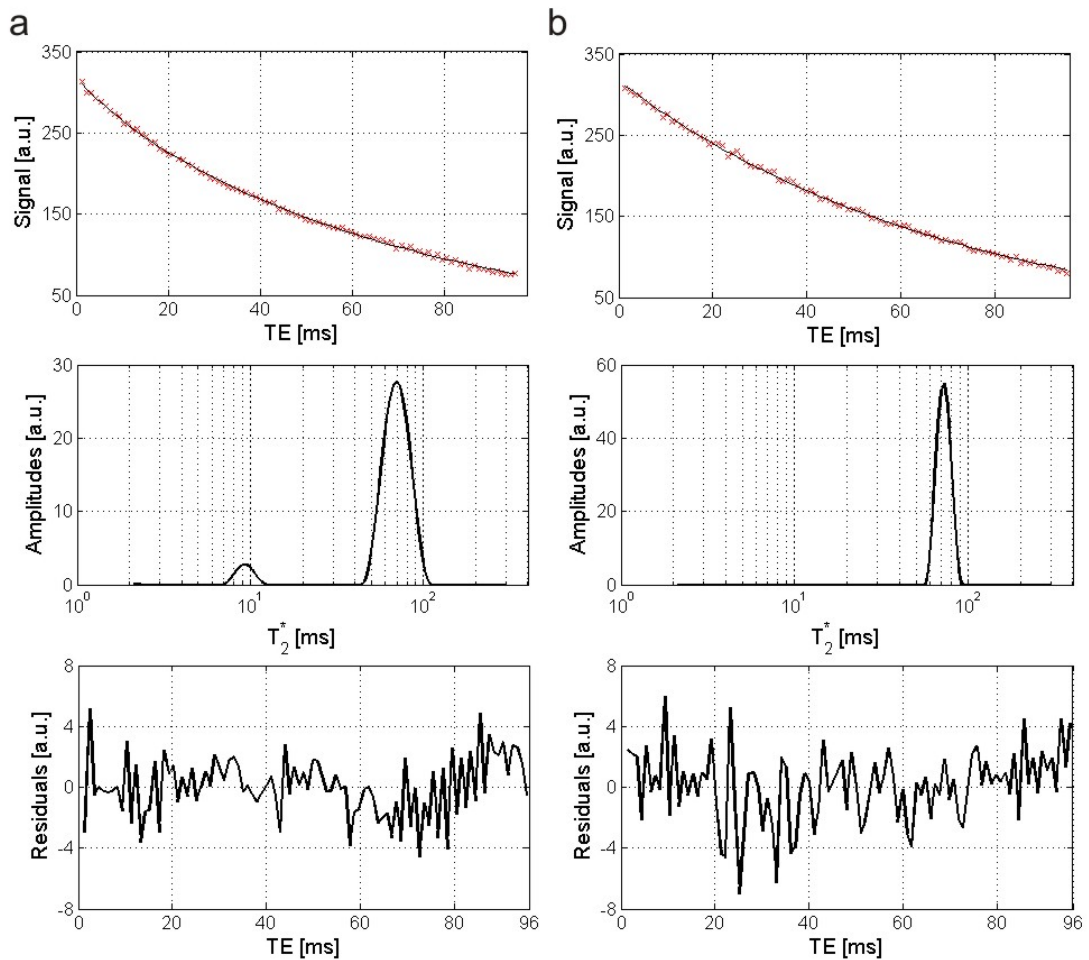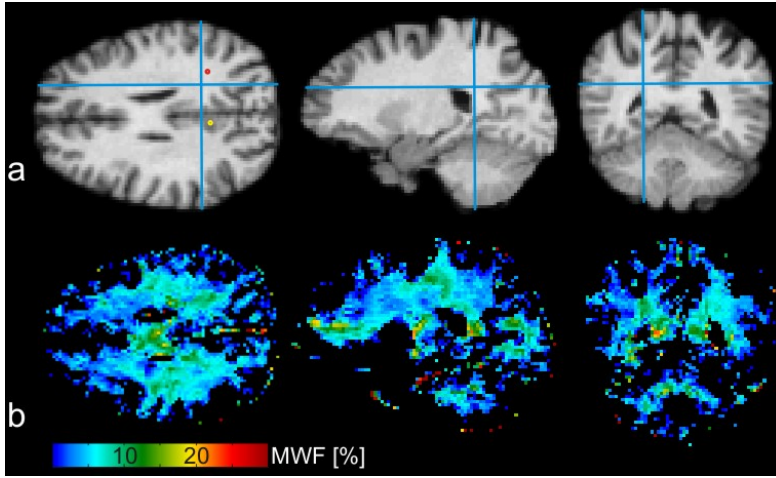
Figure 3.3: *a: Axial, sagittal and coronal MPRAGE images from one healthy subject. The blue lines indicate the location of the respective views. **b:** Corresponding pixelwise sample images showing MWF parameter fit results. The corresponding mGRE images with different echo times can be found in figure 3.1.*

3.3.2   MS patient results

Figure 3.5 presents results from three MS patient investigations. The pixelwise *MWF* parameter maps are shown in figure 3.5d. Regions of prominent MS lesions show reduced *MWF* values in the parameter maps with $MWF \rightarrow 0\%$. These results strongly correlate with previously reported *MWF* behavior in MS lesions [19, 21, 22] and thereby quantitatively confirm the severe demyelination within the lesions.

Table 3.1 shows the mean *MWF* for various WM structures from all investigated subjects (healthy volunteers and MS patients) together with the corresponding standard deviations (SD) and the total number of pixels found in the respective region. The averaged *MWF* value over all subjects yields 6.9%. Statistical analysis using a two-tailed Student's t-test was performed to study differences between regions. Despite the high SD's of the single WM areas, all regions have significantly different *MWF* values (p < 0.001 for all regions, except p = 0.01 for the difference between the splenium and the genu of the corpus callosum). However, when comparing volunteers and patients separately, no significantly lower *MWF* values can be observed for the MS patients in comparison to the healthy subject results. The obtained *MWF* values of this study correspond to literature values [9, 16, 19, 21, 22, 36, 45, 60, 71], but remain in the lower range of published quantitative myelin water data.
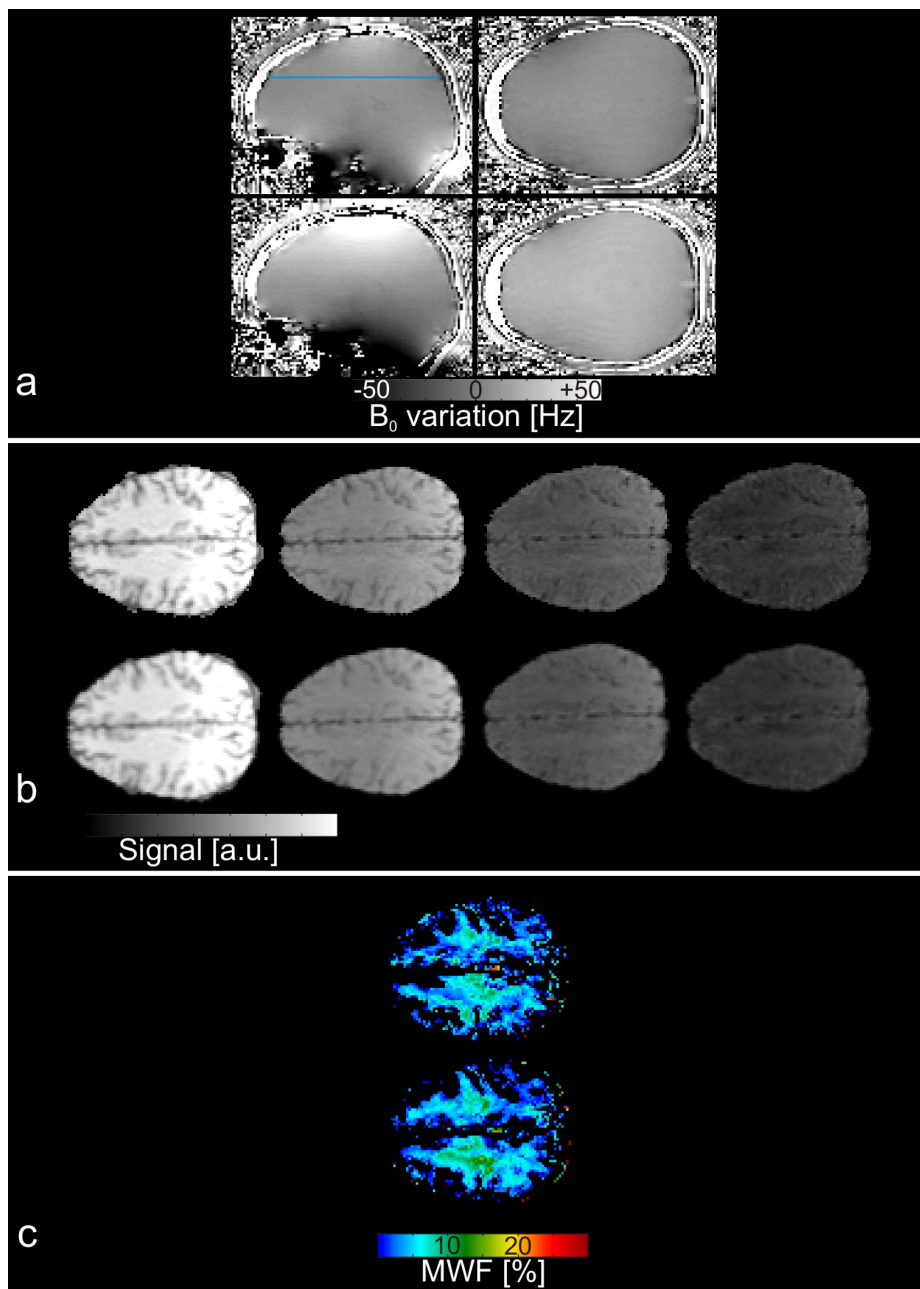
Figure 3.4: ***Top row:*** *Regular measurement protocol.* ***Bottom row:*** *Manually induced increase of the B_0 inhomogeneity by 10 $\mu T/m$ (in z-direction from top to bottom).* ***a:*** *B_0 maps. Sagittal: Illustration of the field variation in z-direction. Axial: Evaluated slice that is far from natural sources of B_0 inhomogeneity. The blue line shows the exact location of the axial view.* ***b:*** *Corresponding mGRE images representing echoes number 1, 32, 64 and 96.* ***c:*** *Pixelwise MWF parameter maps. The induced main magnetic field gradient leads to an overestimation of the MWF and a loss of white matter contrast.*
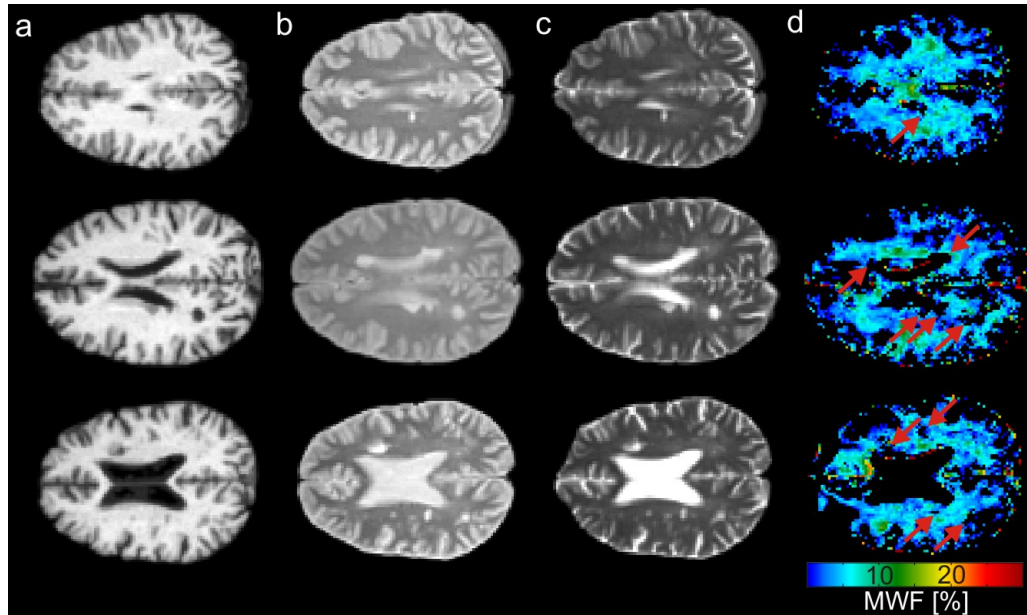
Figure 3.5: *Pixelwise results of three MS patients showing one representative axial view per patient.* **a:** T_1*-weighted MPRAGE image.* **b:** *PD-weighted image.* **c:** T_2*-weighted image.* **d:** *Corresponding sample images showing MWF parameter fit results. Regions of most prominent MS lesions are indicated with red arrows.*

Table 3.1: *The mean MWF [%] for various WM structures derived from pixelwise results of all subjects (healthy volunteers and MS patients). Standard deviations (SD) and the total number of pixels from the respective region are listed in addition.*

Structure	Mean MWF [%]	SD	Number of pixels
Minor forceps	4.6	3.1	693
Major forceps	6.6	3.3	876
Genu of corpus callosum	8.1	6.8	549
Splenium of corpus callosum	8.9	5.5	906
Internal capsules	5.6	4.4	372
Average white matter	6.9	5.0	3396

3.4   Discussion

In this work, a solution to 3D in vivo myelin water imaging was presented, which uses mGRE pulse sequences at 1.5 T for data acquisition and an NNLS algorithm for analysis of the multi-component T_2^* relaxation. The proposed 3D procedure offers not only whole brain coverage, but also a clinically feasible scan time of less than 10 minutes for the acquisition of 96 different echo times. Due to the high number of acquired echoes, the short first echo time and the short echo spacing of the mGRE sequence, an accurate sampling of the T_2^* relaxation and especially the fast myelin water signal decay could be achieved.

Obtained MWF results (averaged WM $MWF = 6.9\%$) correspond to previously published values [9, 16, 19, 21, 22, 36, 45, 60, 71, 76], but remain in the lower range of myelin water literature. So far, there is little work published on myelin water imaging based on mGRE sequences: Du et al. received 11% for the averaged WM MWF [21] and Hwang et al. 10.2% [60]. For both publications and in contrast to this work, measurements were conducted at field strength of 3 T. At first sight, the low resulting MWF values of this study seem to be surprising. However, other MWF publications have shown discrepancies between results from 1.5 T and 3 T [71, 76]. Both Oh et al. [71] and Kolind et al. [76] found significantly lower MWF at 1.5 T than at 3 T, which were attributed to dielectric effects at 3 T producing B_1 inhomogeneity issues or higher SNR at 3 T that improve the detectability of the short components. Hence, the low detected myelin water values of this study might be due to the low field strength. Further measurements that compare results between 1.5, 3 and 7 T would be needed to clarify this point.

Despite the high standard deviations found for the different WM regions, the resulting mean MWF values show significant differences between the investigated structures (for example MWF in the minor forceps $\sim 50\%$ of the MWF detected in the splenium of the corpus callosum). However, no significant difference between healthy subjects and MS patients could be found. Possible explanations for this could be a too low population of healthy volunteers or a patient population with a high amount of normal appearing white matter.

For the MS patients, regions of prominent MS lesions show reduced MWF values in the parameter maps with $MWF \to 0\%$. Therefore, the proposed technique of this study is able to show demyelination within MS lesions. However, the obtained MWF values $\to 0\%$ in all the lesions (similar to the behavior in GM), which complicates an exact characterization and differentiation of lesions and prevents detailed investigation of ongoing processes within lesions, like for example remyelination. Moreover, the 3D acquisition scheme proposed in this work uses a relatively low isotropic resolution of ~ 2 mm, which additionally impedes MS lesion detection and small lesions might therefore be missed in the quantitative analysis. Nevertheless, a too homogenous MS patient population with completely demyelinated

lesions could account for the *MWF* values seen in this work. To conclusively clarify the clinical usefulness of the proposed method, a higher patient population and a correlation to histopathological results would be needed.

Dealing with main magnetic field inhomogeneities is an important topic in mGRE imaging. The presence of macroscopic field inhomogeneities can cause artifacts in gradient-echo images and can lead to substantially different intensities of the same tissue class at different positions in an image. Accurate determination of T_2^* values, as well as quantification of myelin water might therefore be impaired by main magnetic field inhomogeneities. To circumvent issues with static field inhomogeneities, measurements of this study were conducted at low field strength and a second order manual shim was performed prior to the mGRE acquisition. Acquisitions with an additionally superimposed static magnetic field gradient have shown that improper shimming can lead to a non-exponential signal modulation and result in an overestimation of *MWF* values. Nevertheless, measurements at higher field strengths would in principle benefit from higher SNRs. But the stronger B_0 inhomogeneities might then lead to severe changes of the signal decay and would hence complicate a reliable quantitative data analysis. A more detailed discussion on B_0 inhomogeneities at higher field strength and their influence on myelin water imaging based on mGRE pulse sequences can be found in chapter 4.

T_1 weighting is another important error source that could impair an accurate detection of the myelin water fraction in this study. Because of the short repetition time chosen for the mGRE setup (98 ms), the resulting signal experiences potential multi-component T_1 weighting. The myelin water pool was shown to have a shorter T_1 than the intra- and extracellular compartment [10–13]. The existence of the multi-component T_1 relaxation could lead to higher T_1 saturation of the intra- and extracellular component in the mGRE protocol and might finally result in an overestimation of the *MWF*. To clarify this point, a separate measurement at low flip angle of 10° was conducted on one healthy subject, assuming that the mGRE signal based on $TR = 98$ ms and $\alpha = 10°$ is approximately independent of T_1 influences. The resulting *MWF* parameter maps were compared to the corresponding maps derived from the standard experimental setup (data not shown). The averaged *MWF* found for $\alpha = 10°$ were $\sim 5\%$ lower than the *MWF* derived from the standard measurement. However, the observed difference was not statistically significant, thereby indicating that T_1 effects play a minor role in the applied mGRE protocol and the resulting myelin water maps.

In order to investigate the influence of intercompartmental exchange on the acquired mGRE data sets, numerical simulations based on a two pool model were performed as described in section 2.3. Thereby, the mGRE pulse sequence was simulated based on two T_2^*, two T_1, $MWF = 8\%$ and an exchange rate of $k = 5$ s^{-1}. The resulting signal intensities were compared to the case of neglected exchange and showed a signal difference of 2% in maximum. This outcome indicates that the timescale of proton exchange is too long for having a strong influence on

the measured T_2^* distributions and the myelin water fractions derived from mGRE acquisitions.

In contrast to the publications by Du et al. [21] and Hwang et al. [60], where a fixed three-pool WM model was applied for quantitative T_2^*-based *MWF* analysis, the NNLS algorithm used in this study requires no a-priori knowledge about the number of components present. Application of the fixed three-pool model benefits from additional fitting of the myelinated axon water pool, which can give insight into the axonal integrity of MS lesions. Nevertheless, distinction of three water pools was not feasible in this study, because T_2^* distributions with three isolated peaks could not be observed in the course of the data analysis. The most reliable fit results could be produced by splitting the distributions into two pools: a myelin water part and an intra- and extracellular water part.

Recently, Deoni et al. introduced a new, fast 3D method for mapping the *MWF* that is based on SPGR and bSSFP sequences [13]. In 16 to 30 min, a whole brain multi-component quantification is feasible with this technique. The big advantage of the proposed procedure is the possible quantification of all parameters defining the two pool model, like T_1, T_2, *MWF* and exchange rate. However, in contrast to this study, a complex hybrid approach consisting of a genetic algorithm and a local search method has to be applied for the parameter fitting. Moreover, the acquisition time is approximately double as long as our scan time, while only 18 different points are measured as opposed to the 96 different echoes of the method presented in this chapter.

3.5   Conclusion

A new solution to in vivo myelin water imaging based on 3D T_2^* mapping was presented. The procedure proposed in this work offers not only whole brain coverage, but also clinically practicable acquisition times. The results for the myelin water fraction are in the lower range of previously reported values and are able to show demyelination in MS lesions. However, the clinical application remains questionable. Further measurements are needed that clarify the possibility of characterizing MS lesions and detecting remyelination and other ongoing processes inside the lesions.

Chapter 4

Myelin water imaging at high field strength using mGRE sequences

4.1 Introduction to B_0 inhomogeneities

As already briefly covered in the previous chapter, a major drawback of gradient-echo imaging is its inherent sensitivity to static magnetic field variations. In general, the signal formation in GRE imaging depends on the natural microscopic T_2 relaxation and a second term that describes the additional dephasing arising from inhomogeneous static magnetic field contributions. Static magnetic field inhomogeneities can be divided into mesoscopic and macroscopic variations. On the one hand, mesoscopic inhomogeneities result from susceptibility differences between biological tissues and can provide information about tissue structure and function [77]. On the other hand, macroscopic perturbations arise from magnet imperfections, air-tissue boundaries or ferromagnetic objects and are usually undesired in MR imaging, because they do not provide structural or physiological information. In fact, macroscopic variations can lead to image distortions and signal loss in gradient-echo imaging [77, 78].

In chapter 3, problems related to macroscopic field inhomogeneities could successfully be avoided by conducting the mGRE experiments in 3D at low field strength and by performing a second order manual shim prior to the acquisition. Nevertheless, moving to higher field strengths would be attractive in order to profit from the increased SNR. However, severe disturbance of the two-pool T_2^* decay has to be expected at high field strength due to stronger B_0 inhomogeneities and the manual shimming procedure might not be adequate to eliminate the present field variations.

There exist several strategies to minimize the effects of macroscopic field variations in gradient-echo imaging. Thereby, one has to differentiate between 2D and 3D imaging. In 2D GRE imaging, the voxel dimension in the slice-select direction is typically larger than the in-plane voxel size and is therefore particularly sensitive to field inhomogeneities [79]. For macroscopic variations, where the scale of the inhomogeneities is larger than the voxel size, background magnetic field variations are considered as constant inside a voxel and can be approximated as stationary gradients perpendicular to the slice plane [78]. The presence of a local background field gradient in slice select direction induces additional non-exponential signal modulation in gradient-echo data sets and can be modeled as a sinc function [77, 80]:

$$S(t) = S_0(t) \cdot sinc\left(\gamma G_z \frac{\Delta z}{2} t\right), \tag{4.1}$$

where $S(t)$ are the measured signal intensities, $S_0(t)$ is the pure signal without background field gradient, γ is the gyromagnetic ratio, Δz is the slice thickness and G_z is the background field gradient. For explicit correction of the B_0 inhomogeneity in this case, G_z can either be determined from a B_0 field map or can directly be estimated from fitting equation 4.1 based on multiple GRE acquisitions. The sinc correction was successfully applied by Hwang et al. to correct 2D mGRE data

sets prior to myelin water quantification [60]. However, it can only be applied to correct background gradients parallel to the slice-select direction in 2D gradient echo acquisitions [80].

Another possibility for correcting 2D gradient-echo data sets is z-gradient compensation, also called z-shimming. This technique was introduced by Frahm et al. [79] and was mainly applied to correct 2D echo-planar imaging data sets used for functional MRI [81]. The z-shimming technique assumes as well (similar to the offline sinc correction described above) linearity of the background field gradient across the slice and proposes to rewind the additional phase with the appropriate gradient offset on the slice-select rephase lobe. In case multiple data sets are collected with different z-gradient offsets, each acquisition will compensate for a different amount of phase dispersion [81]. Section 4.2 of this chapter introduces a new approach for quantitative myelin water imaging based on z-shimming applied to correct B_0 inhomogeneities in 2D mGRE pulse sequences at 3 T.

In principle, the acquisition of 3D gradient-echo data sets helps to eliminate severe macroscopic field variations because of the increase in resolution compared to 2D techniques [78]. As a matter of fact, the results from chapter 3 (fig. 3.1) indicate that the 3D mGRE acquisition scheme offers high image quality without image distortions or signal voids arising from B_0 inhomogeneities. Despite the convincing performance at 1.5 T, the complete elimination of macroscopic field variations is not perfectly feasible in 3D acquisitions at higher field strength. Section 4.3 of this chapter clearly delineates the signal modulations arising from B_0 perturbations at 3 T and their impacts on derived myelin water fraction values. Unfortunately, the sinc correction described above can only be applied for the correction of background gradients parallel to the slice-select direction in 2D acquisitions. The only known correction scheme for 3D GRE acquisitions is 3D gradient compensation, which was introduced by Posse et al. [82]. However, this technique is clinically impractical due to too long scan times.

4.2   Myelin water imaging based on z-shimmed 2D mGRE pulse sequences at 3T

4.2.1   Introduction

In this section, a new approach to myelin water imaging is presented that is based on 2D multi-gradient-echo pulse sequences at 3 T. Z-shimming is performed to correct main magnetic field inhomogeneities. Results from measurements of healthy subjects are presented and the influence of B_0 inhomogeneities on the derived myelin water fraction values is discussed.

4.2.2 Methods

Experiments were conducted on 3 healthy volunteers using a whole-body 3 T MRI system (Magnetom Verio, Siemens Healthcare, Erlangen, Germany) based on a single slice with axial orientation, image matrix 192 x 144, 1.5 x 1.5 mm^2 in-plane resolution and a slice thickness of 4 mm. The protocol for quantitative *MWF* estimation consisted of:

- A carefully conducted second-order manual shim for correction of main magnetic field inhomogeneities resulting in frequency variations of less than 25 Hz within the shimmed volume containing the whole brain.

- An MPRAGE sequence for anatomical reference (*TR/TE* = 2000/3.6 ms, inversion time *TI* = 1000 ms, flip angle $\alpha = 8°$, bandwidth = 180 Hz/pixel).

- A T_2^* weighted mGRE pulse sequence with alternating readout gradient polarities and RF spoiling. The phase-encoding gradients were rewound at the end of each echo train. 64 different echoes were recorded with a first echo time of 2.0 ms and an echo spacing of 1.45 ms. Moreover, TR was 350 ms, the flip angle was chosen to be 46° and 2 averages were acquired per image. The mGRE sequence was repeated 12 times with different z-shim acquisitions having nominal z-gradient refocusing lobes varying between 40 and 150% [79]. The total scan time for all z-shimmed mGRE acquisitions was 17 minutes.

For registration of the MPRAGE and different z-shimmed mGRE data sets, the software packages FSL [68] and AFNI [69] were used. Offline data analysis was performed using Matlab 2007b (The MathWorks, Inc., Natick, MA, United States). Adjacent mGRE acquisitions were combined using the square root of the sum of squares method [81]:

$$I_{comp} = \frac{\sqrt{I_c^1 + I_c^2 + \ldots + I_c^N}}{N},$$
(4.2)

where I_c^N are the N uncompensated mGRE data sets. Additionally, a median filter with kernel size 3 was applied to the compensated mGRE images before fitting [73]. The resulting T_2^* decays were analyzed using the regularized NNLS algorithm described in section 3.2.

4.2.3 Results

Figure 4.1 illustrates exemplary acquired 2D mGRE images of one healthy subject. The illustrated time series represents images acquired at echo times 2.0, 47.0 and 93.4 ms. The uncompensated images depict severe signal loss and signal voids, which are mainly present at the late echoes. The z-shimming technique, on the other
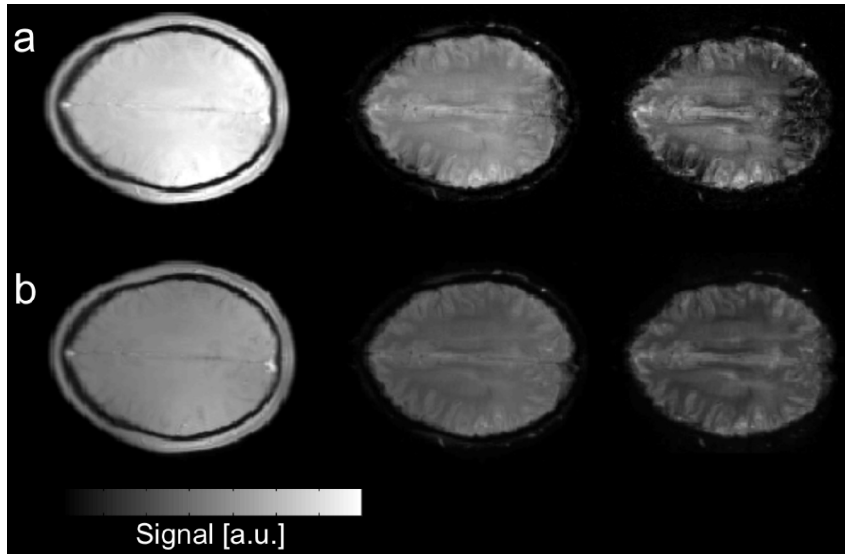
Figure 4.1: *Exemplary 2D mGRE images of one healthy subject representing echoes number 1, 32 and 64 with corresponding echo times of 2.0, 47.0 and 93.4 ms.* ***a:*** *Uncompensated images based on a z-gradient refocusing lobe of 100%.* ***b:*** *Compensated z-shimmed images. The signal loss and signal voids present in the uncompensated images could successfully be corrected with the z-shimming technique. The signal intensities of the late echoes had to be increased for illustration purposes.*

hand, could successfully reduce the issues related to macroscopic field variations and no artifacts or signal voids are present in the compensated data (fig. 4.1b).

The influence of B_0 inhomogeneities on the acquired T_2^* decay is shown in figure 4.2, where a single-pixel fitting example is presented. For the case of the uncompensated mGRE data set, the present B_0 inhomogeneities lead to non-exponential signal modulations resulting in the detection of only one component by the NNLS algorithm. Furthermore, the resulting fit residuals yield high values up to 20% of the measured signal intensities and highlight thereby the modified curve behavior that is neither purely biexponential, nor purely monoexponential. In contrast to the uncompensated T_2^* decay, the NNLS algorithm is able to detect myelin water in the z-shimmed data and an *MWF* of 4.5% is found for the WM pixel (fig. 4.2b). In addition, excellent correspondence between the z-shimmed data points and the fitted signals, yielding residuals $< 2\%$, can be observed. One might as well notice a shortening of the T_2^* values compared to the results from the measurements performed at 1.5 T presented in chapter 3. The maxima of the obtained T_2^* peaks in chapter 3 were found to be 10 ms for the myelin water pool and around 70 ms for the intra- and extracellular component (fig. 3.2). In contrast, the maxima of the T_2^* distribution found in this section yield 4 ms for myelin water and 50 ms for the intra- and extracellular component respectively and reveal the strong spin dephasing being present at higher field strength.
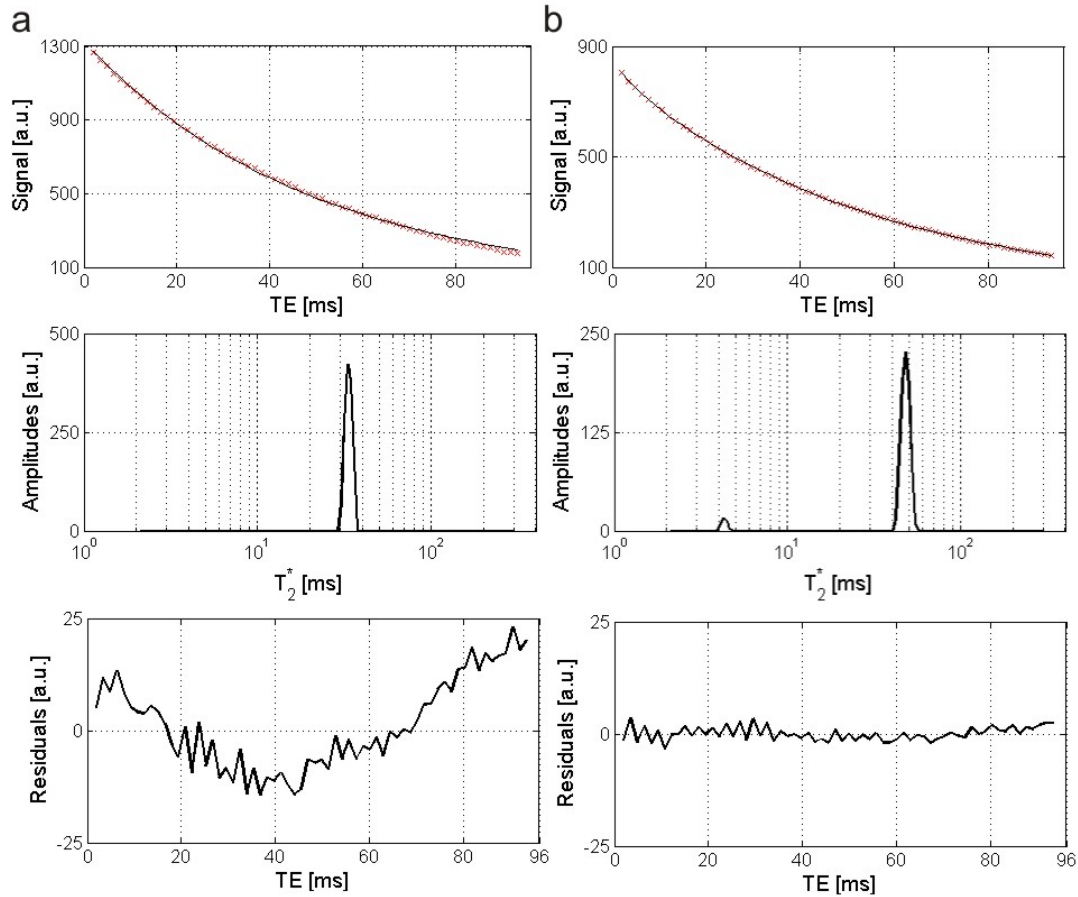
Figure 4.2: *Introductory fit example of one WM pixel from a healthy subject.* ***a:*** *Fit based on uncompensated data with z-gradient refocusing lobe of 100%.* ***b:*** *Fit based on z-shimmed data set.* ***Top:*** *Acquired T_2^* decay curve (red crosses) and fitted signal using NNLS algorithm (black line).* ***Center:*** *Corresponding regularized T_2^* distribution.* ***Bottom:*** *Fit residuals. Location of the WM pixel is illustrated in figure 4.3a in red (data set on top).*

Figure 4.3: *a: MPRAGE images from three healthy subjects. The red dot in the upper data set illustrates the location of the WM pixel evaluated in figure 4.2. b: Corresponding pixelwise sample images showing MWF parameter fit results from the uncompensated data sets with z-gradient refocusing lobe of 100%. c: Corresponding MWF parameter maps based on the z-shimmed mGRE data sets.*

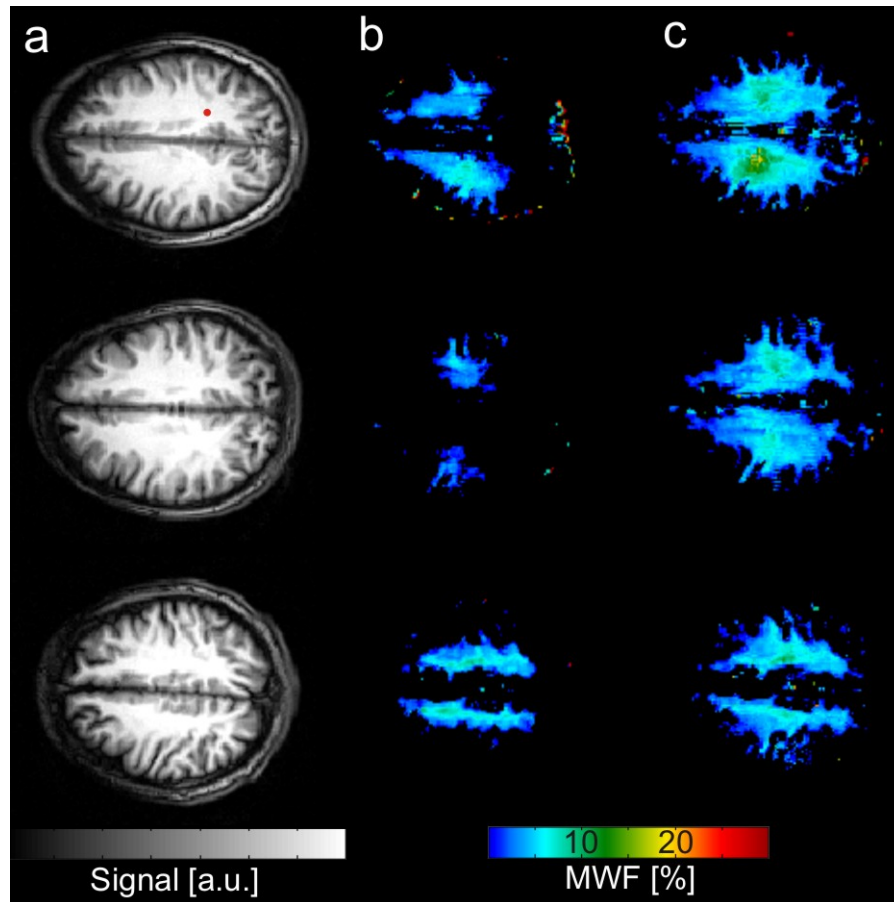Pixelwise *MWF* parameter maps of three healthy volunteers are illustrated in figure 4.3. The derived *MWF* parameter maps based on the uncompensated data confirm the results from the single pixel fitting given above and indicate the failure of the NNLS algorithm in detecting the myelin water compartment due to the signal modulations originating from B_0 inhomogeneities. In contrast, the myelin water maps depicted in figure 4.3c demonstrate the effective B_0 correction based on z-shimming. The resulting maps appear smooth and a good qualitative correspondence with the WM regions of the MPRAGE images is obtained. Similar to the pixelwise results from chapter 3, the fit procedure only detects myelin water in WM pixels, whereas the *MWF* in GM yields zero. Nevertheless, the resulting *MWF* in fronterior and posterior WM remain low ($\sim 1-2\%$) and point out conceivable imperfections of the z-shimming procedure.

4.2.4   Discussion and conclusion

In this section, a solution to in vivo myelin water imaging was presented, which uses 2D mGRE pulse sequences at 3 T and z-shimming for correction of static magnetic field inhomogeneities. Similar to chapter 3, an NNLS algorithm was applied for the analysis of the acquired T_2^* decay. The detection of myelin water could effectively be improved with the z-shimming procedure.

The resulting MWF parameter maps correspond to the obtained maps from chapter 3. However, in fronterior and posterior white matter, the derived myelin water fraction values remain low ($1 - 2\%$). Possible imperfections in the B_0 correction scheme could account for this behavior. Moreover, the mean MWF value obtained here (mean $MWF = 3.9 \pm 2.8\%$) is not higher than the one based on 1.5 T experiments from chapter 3, as to be expected from multi-spin-echo publications [71, 76]. Not only imperfect z-shimming, but also the shortening of T_2^* values could explain this discrepancy. Due to strong spin dephasing at 3 T, a reduced myelin water T_2^* value of ~ 5 ms was observed in this study. Even with the application of mGRE pulse sequences, the detection of this short component is impaired, because the signal will only be present in a few early echoes. This outcome suggests that myelin water imaging using mGRE pulse sequences in general is complicated at high field strength, not only because of macroscopic field variations, but also because of mesoscopic inhomogeneities that substantially decrease the T_2^* relaxation times.

Furthermore, the long acquisition times required for measuring the different z-shimmed mGRE data sets and the low volume coverage due to the single-slice technique represent additional problems related to the procedure introduced in this section. The scan times could indeed be reduced by decreasing the TR and the number of z-shim acquisitions, but the technique will still be limited to a small 2D volume.

In conclusion, macroscopic field inhomogeneities could effectively be corrected with the z-shim technique and the resulting myelin water maps correspond to the results from the previous chapter. But, the clinical application of the introduced procedure is limited due to the low volume coverage and especially the shortening of T_2^* values that impairs an accurate detection of the myelin water pool.

4.3   Myelin water imaging based on 3D mGRE pulse sequences at 3T

4.3.1   Introduction

In this section, the feasibility of myelin water imaging at 3 T using the 3D procedure introduced in chapter 3 is evaluated. Results from measurements of healthy subjects are presented and the effects of field variations on the calculated *MWF* are discussed.

4.3.2   Methods

Measurements were conducted on 2 healthy volunteers using a whole-body 3 T MRI system (Magnetom Verio, Siemens Healthcare, Erlangen, Germany). Thereby, the complete experimental setup from chapter 3 with all settings and parameters was repeated at the higher field strength. The conducted second-order manual shim at 3 T resulted in frequency variations of less than 25 Hz within the shimmed volume containing the whole brain. Furthermore, the postprocessing and analysis procedure described in chapter 3 was analogously applied to evaluate the 3 T 3D mGRE data sets.

4.3.3   Results

Figure 4.4a depicts exemplary acquired 3D mGRE data of one healthy subject. The illustrated time series represents images acquired at echo numbers 1, 32, 64 and 96. As expected from the 3D acquisition scheme using a high readout bandwidth, no image distortions are present in the data. In addition, the high quality of the manual shimming procedure leads to an absence of signal voids in the illustrated images. However, the corresponding myelin water map (fig. 4.4c) depicts the failure of the NNLS algorithm to detect the myelin water component in a significant number of white matter pixels. This behavior is attributed to severe B_0 inhomogeneity issues, as described in section 4.2.

Figure 4.5 shows single pixel fitting examples. For one pixel being located at the center of the axial view (fig. 4.5a), excellent correspondence between the measured data points and the fitted signals is found and the algorithm is able to detect the short myelin water component (resulting $MWF = 3.8\%$). Similar to the results presented in the previous section of this chapter, a shortening of the T_2^* values can be observed in addition. For the second examined WM pixel (fig. 4.5a), the signal modulation due to B_0 inhomogeneities is more pronounced and the acquired
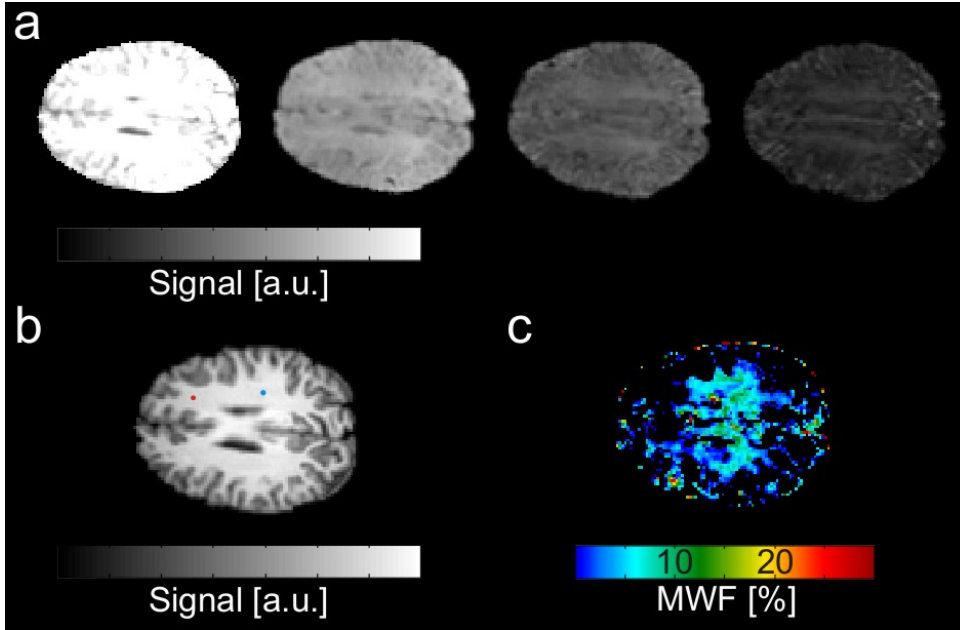
Figure 4.4: *a: Exemplary axial mGRE images of one healthy subject representing echoes number 1, 32, 64 and 96 with echo times of 1.4, 32.1, 63.8 and 95.5 ms. b: Corresponding MPRAGE image. The blue and red dots indicate the positions of the WM pixels from figure 4.5. c: Corresponding pixelwise sample image showing MWF parameter fit results.*

signal decay is no longer biexponential, nor monoexponential (residuals yield 30% in maximum).

4.3.4   Discussion and conclusion

In this section, the 3D mGRE procedure introduced in chapter 3 was applied at 3 T. Results prove that the complete elimination of macroscopic B_0 inhomogeneity contributions is not feasible in 3D acquisitions at high field strength. Strong signal modulations due to macroscopic B_0 variations lead to non-exponential signal behavior and failure of the NNLS algorithm in detecting the myelin water pool. Moreover, reduced myelin water T_2^* values could be observed that strongly impair the accurate detection of the myelin water pool.

In chapter 3, a small, manually induced increase of the B_0 inhomogeneity by 10 μT/m in z-direction was resulting in an overestimation of the *MWF* values, because of an artificial increase of the curve slope at the early echoes. In this section, the signal alterations due to the presence of macroscopic B_0 inhomogeneities are more severe and lead to the destruction of the exponential curve behavior in a significant number of investigated pixels.

The results from this section support the conclusion from section 4.2 and prove
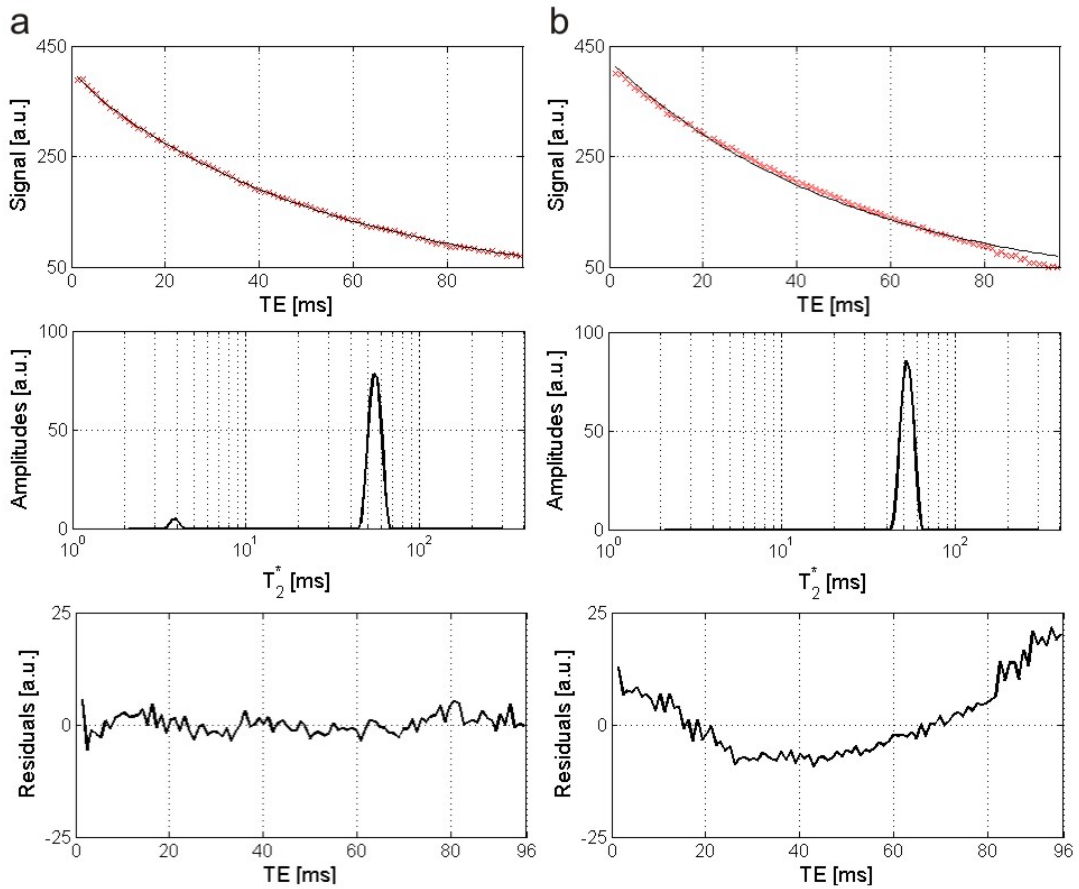
Figure 4.5: *Introductory fit example of two WM pixels from a healthy subject.* **Top:** *Acquired T_2^* decay curve (red crosses) and fitted signal using NNLS algorithm (black line).* **Center:** *Corresponding regularized T_2^* distribution.* **Bottom:** *Fit residuals.* **a:** *Location of pixel indicated in figure 4.4b in blue.* **b:** *Location of pixel indicated in figure 4.4b in red.*

the limitations of myelin water quantification based on mGRE pulse sequences at 3 T. Both macroscopic and mesoscopic field variations impede the myelin water detection at high field strength. Since the 3D gradient compensation procedure is too time consuming [82] and no explicit 3D correction scheme is known from literature, quantification of myelin water based on mGRE pulse sequences should ideally be conducted at low field strength of 1.5 T.

Chapter 5

Simultaneous B_1 and B_0 imaging

5.1   Introduction

The previous chapters impressively demonstrated the importance of B_1 and B_0 imaging for accurate myelin water quantification. In particular for the procedure introduced in chapter 2, mapping of the B_1 and B_0 variance turned out to be crucial in order to obtain reliable MWF results based on bSSFP pulse sequences. Thereby, B_1 field maps were acquired to correct flip angle deviations. Furthermore, B_0 maps were reconstructed to check the quality of the manual shimming procedure, because bad shimming was demonstrated to result in high MWF gradients in the parameter maps.

However, the conventional B_1 and B_0 mapping sequences initially used in chapter 2 required approximately 4 minutes scan time. Especially for the application in clinical routine, shortening of scan time would be attractive in order to have a larger time frame for the acquisition of the myelin water quantification protocol. Therefore, this chapter introduces a new method for fast simultaneous B_1 and B_0 imaging that resembles the approach presented by Amadon et al. [83]. For the implementation of the sequence, a free scripting framework was used that simplifies online postprocessing of the reconstructed data and enables direct visual inspection of the B_1 and B_0 variation on the scanner console [84]. As a consequence, the quality of the manual shimming procedure can be evaluated before starting the myelin water quantification sequence.

Actual flip angle imaging (AFI) has originally been introduced as a fast and robust 3D method for mapping the B_1 transmit field by measuring the spatial variations of the effective flip angle [85]. The AFI pulse sequence consists of a dual TR conventional spoiled gradient echo pulse sequence, where $TR_2 > TR_1$. For the technique introduced in this chapter, a second echo has been added to the implementation of the standard AFI timing diagram. The acquisition of the additional echo enables B_0 mapping by reconstructing phase difference maps based on the complex information of the two acquired echoes. The proposed sequence scheme offers therefore simultaneous B_1 and B_0 imaging based on dual-echo AFI. In vivo results of fast B_1 and B_0 mapping are presented in the course of this chapter.

5.2   Methods

The timing diagram of the modified AFI sequence enabling both B_1 and B_0 mapping is illustrated in figure 5.1. Assuming complete spoiling of the transverse magnetization and TR shorter than the longitudinal relaxation time, the flip angle α (and thereby the final B_1 maps) can be calculated according to the signals S_1 and S_3 with [85]:
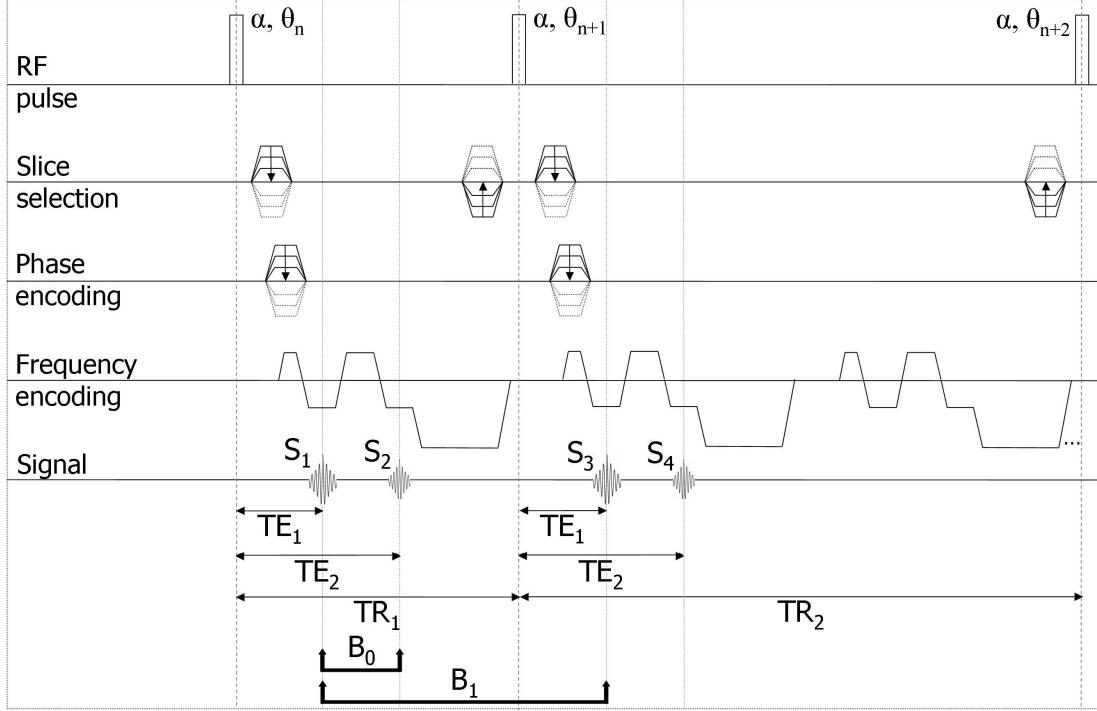
Figure 5.1: *Schematic timing diagram illustrating the implemented 3D dual-echo AFI pulse sequence.*

$$\alpha \approx \arccos\left(\frac{r \cdot n - 1}{n - r}\right), \quad with \quad r = \frac{S_3}{S_1} \quad and \quad n = \frac{TR_2}{TR_1}. \tag{5.1}$$

In order to achieve complete elimination of the transverse magnetization at the end of TR, the RF spoiling scheme proposed in [86] was incorporated in the sequence. Moreover, high gradient spoiling of $122 \cdot 2\pi$ across a voxel was implemented in read-out direction for the first TR and the read-out gradients for the second TR were applied $n = TR_2/TR_1$ times (fig. 5.1) [86].

B_0 maps were reconstructed according to the magnitudes and phases of the signals S_1 and S_2 by using the four-quadrant arctangent function [74]:

$$\Delta\phi = \arctan 2\left[Im(Z_1 Z_2^*), Re(Z_1 Z_2^*)\right], \tag{5.2}$$

$$with \quad Z_{1,2} = r_{1,2}exp(i \cdot \varphi_{1,2}),$$

where $\varphi_{1,2}$ depict the phases and $r_{1,2}$ the magnitudes of $S_{1,2}$.

Experiments were performed on the brains of healthy volunteers using a 1.5 T MRI system (Magnetom Avanto, Siemens Healthcare, Erlangen, Germany) and a 12-channel phased-array head coil. The DE-AFI sequence was based on a 3D matrix of 64 x 64 x 20, 4 x 4 x 8 mm^3 resolution and non-selective excitation. Moreover, the following parameters were chosen: $TR_1 = 35$ ms, $TR_2 = 175$ ms, $TE_1 = 2.33$ ms, $TE_2 = 7.09$ ms, $\alpha = 30°$ and RF spoiling phase increment = 50°. The total
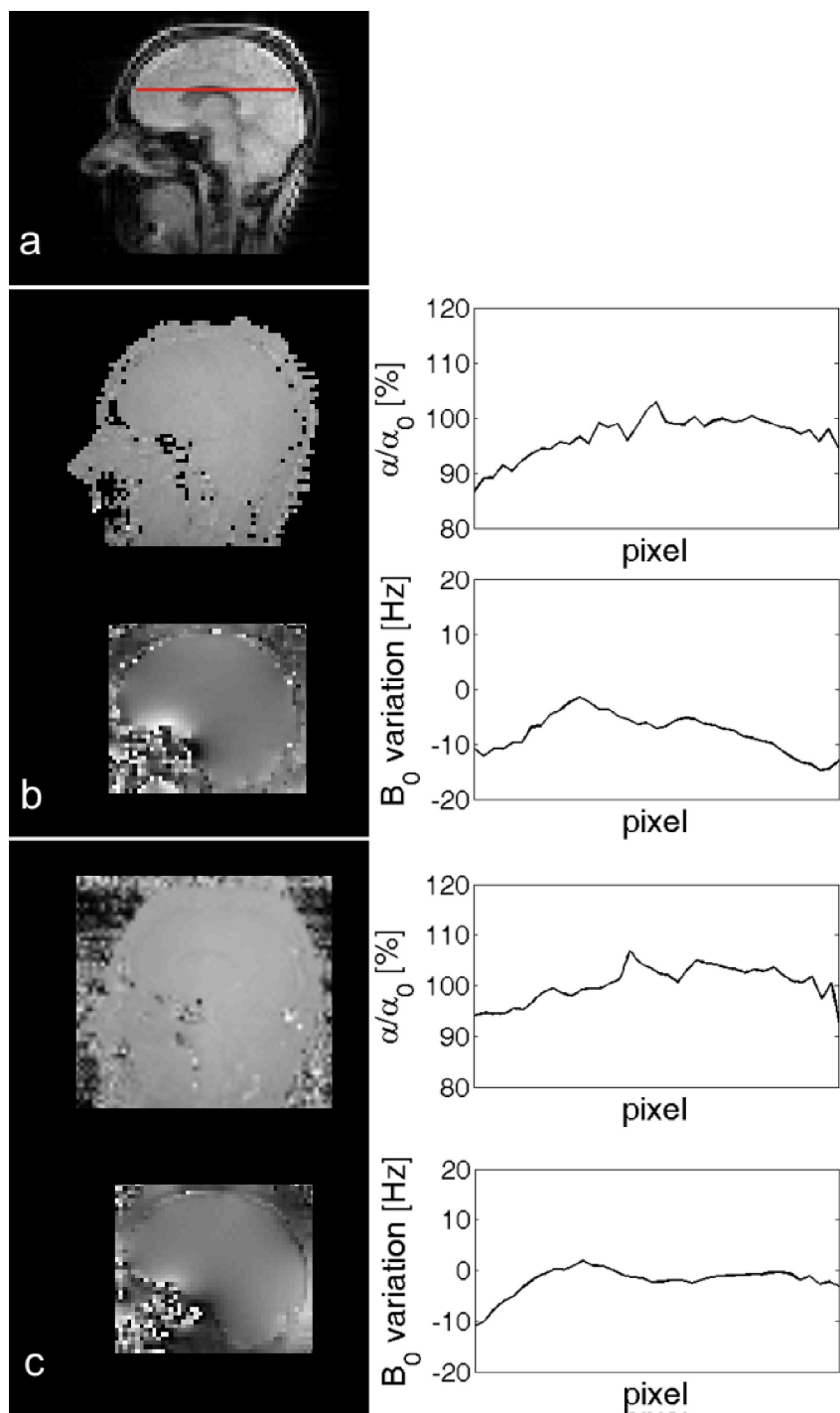
Figure 5.2: *In vivo results showing both B_1 and B_0 maps. **a:** Anatomical image indicating the location of the selected profile (red line). **b:** Representative B_1 (top) and B_0 (bottom) maps acquired with the proposed simultaneous B_1 and B_0 mapping sequence and corresponding profiles on the right side. **c:** B_1 (top) and B_0 (bottom) maps measured with the two separate standard pulse sequences and corresponding profiles.*

scan time for the combined B_1 and B_0 mapping pulse sequence was 134 seconds (without the application of parallel imaging techniques).

In order to validate the proposed technique, two separate standard pulse sequences were measured in addition. For comparison of the B_1 field maps, a triple α scheme, as described in [67], was acquired with similar parameters than the ones indicated above. For comparison of the B_0 field maps on the other hand, a built-in scanner solution was used that as well acquires two gradient echo datasets. The ΔTE of the built-in protocol was similar to the one given above ($\Delta TE = 4.76$ ms).

The postprocessing of the experimental data was implemented online by using the framework described in [84]. The calculated B_1 and B_0 variation could therefore directly be inspected at the scanner console.

5.3 Results

Figure 5.2b presents in vivo B_1 and B_0 mapping results from one healthy subject acquired with the DE-AFI protocol. The resulting B_1 variation looks smooth and yields values close to the reference flip angle (10% deviation in maximum). No artifacts due to improper gradient spoiling can be observed. The calculated deviations remain small in both brain tissue and the ventricular system (see profile) indicating the sucessful elimination of T_1 contributions. Furthermore, the B_1 maps correspond well with AFI results from literature [85, 86] and show no significant discrepancy when comparing to the results derived from the triple α scheme (fig. 5.2c).

Additionally, good correspondence between the resulting B_0 maps using the DE-AFI sequence (fig. 5.2b bottom) and the B_0 maps deduced from the built-in scanner protocol (fig. 5.2c bottom) can be observed. Reconstruction of B_0 maps based on averaging between S_1, S_2 and S_3, S_4 did not lead to an improvement of the maps. Hence, S_4 was not taken into account for neither the calculation of B_0 nor B_1 variations. Besides that, no phase unwrapping was necessary for the calculation of the B_0 variation due to the application of the four-quadrant arctangent function.

5.4 Discussion and conclusion

A new procedure for simultaneous B_1 and B_0 mapping using a dual-echo actual flip angle imaging pulse sequence was presented in this chapter. The proposed technique has the advantages of offering whole brain coverage and a fast acquisition time (134 seconds), which is twice as fast as using separate conventional B_1 and B_0 mapping procedures. Moreover, the simultaneous B_1 and B_0 mapping method yields reliable and robust maps that offer a similar quality compared to the standard approaches.

The presented DE-AFI procedure might therefore provide a real alternative to common B_1 and B_0 imaging techniques and can help to overcome systematic error sources in *MWF* mapping in the future.

Chapter 6

Summary and outlook

6.1 Summary

The myelin water fraction (MWF) is a parameter that directly correlates with the integrity of the myelin sheath and can therefore provide valuable insight into the pathology of white matter diseases. Based on multi-component analysis of non-invasive quantitative MRI measurements, mapping of the MWF becomes feasible. However, the most common myelin water imaging technique, which is based on the application of multi-spin-echo pulse sequences, suffers from a limited volume coverage due to its 2D acquisition scheme and lacks the possibility to accurately sample the fast myelin water signal decay. This thesis focused on the development and application of new myelin water imaging techniques that aim to overcome the major drawbacks related to the conventional MWF mapping procedure.

In chapter 2 of this thesis, the high signal-to-noise ratios and short acquisition times of bSSFP were exploited to implement a fast 3D myelin water imaging technique. Based on modified Bloch equations, an extended bSSFP signal equation was developed that incorporates two-pool characteristics describing brain tissue. The derived bSSFP equation was used to analyze data from in vivo 3D bSSFP measurements with varying flip angles of healthy white matter. The MWF and the signal amplitude were thereby fitted as single unknowns, while a priori assumptions were made for the other parameters (relaxation times and exchange rate) of the two-component system. On-resonance magnetization transfer effects could successfully be excluded from experiments by choosing long RF pulse durations. However, the application of the long pulses required the integration of a finite pulse correction, which was applied to the derived bSSFP signal equation. Moreover, systematic errors due to B_1 inhomogeneities were eliminated by correcting flip angle deviations prior to data analysis and B_0 variations were reduced to a minimum by conducting high order manual shims ahead of data acquisition.

MWF values found in chapter 2 showed good correspondence with results from literature. In addition, the application of bSSFP pulse sequences offers a fast and stable approach to high-resolution 3D myelin water imaging with whole brain coverage. However, the clinical application of the proposed technique is impeded due to the strong dependence of the MWF on the fixed two-pool parameters. Not only the application to pathologies remains questionable, but also the investigation of maturation or ageing of white matter is impaired. Nevertheless, the procedure introduced in chapter 2 provides a non-negligible contribution to the relatively new field of 3D myelin water quantification.

Chapter 3 introduced a 3D acquisition scheme based on multi-gradient-echo (mGRE) pulse sequences that was applied for sampling multi-component T_2^* decay in human brains of healthy subjects and multiple sclerosis patients at 1.5 T. The proposed 3D procedure offers not only whole brain coverage, but also a clinically feasible scan time of less than 10 minutes for the acquisition of 96 echo times. Due to the high

number of acquired echoes, the short first echo time and the short echo spacing of the mGRE sequence, an accurate sampling of the T_2^* relaxation and especially the fast myelin water signal decay could be achieved. A non-negative least squares (NNLS) algorithm was used for analysis of the acquired T_2^* decay. The NNLS algorithm required no a-priori knowledge about the number of existing components and represents therefore an unbiased technique of analyzing multi-exponential data. Quantitative myelin water maps were generated based on analysis of the derived T_2^* spectra. To circumvent issues with static magnetic field inhomogeneities, measurements described in this chapter were conducted at low field strength and a second order manual shim was performed prior to the mGRE acquisition.

Obtained *MWF* results from chapter 3 correspond with previously published values, but remain in the lower range of myelin water literature. Nonetheless, the resulting mean *MWF* values showed significant differences between investigated white matter structures. Additionally, regions of prominent multiple sclerosis lesions show reduced *MWF* values in the parameter maps with $MWF \rightarrow 0\%$. Therefore, the proposed technique is able to denote demyelination within MS lesions. An increased population of healthy subjects and MS patients would be needed to clarify the possibility of characterizing MS lesions and detecting remyelination and other ongoing processes inside the lesions.

Possible adaptations and modifications of the proposed procedure from chapter 3 were covered in chapter 4. Thereby, the major emphasis was on measurements at high field strength and the resulting consequences due to strong B_0 inhomogeneities. In section 4.2, a new approach based on 2D multi-gradient-echo pulse sequences at 3 T was presented that applied z-shimming for correction of main magnetic field inhomogeneities. The detection of myelin water could be improved with the help of the z-shimming method. The resulting *MWF* parameter maps correspond to the obtained values from chapter 3. However, in fronterior and posterior white matter, the derived myelin water fraction values remained low $(1-2\%)$, which could be explained by possible imperfections of the B_0 correction scheme. The clinical application of the introduced procedure is impeded due to the low volume coverage and particularly the decreased T_2^* values at 3 T that hinder an accurate detection of the myelin water pool.

Section 4.3 repeated the 3D measurements from chapter 3 at higher field strength of 3 T. The results supported the conclusion from section 4.2 and proved the limitations of myelin water quantification based on mGRE pulse sequences at high field strength. Both macroscopic and mesoscopic field variations complicated the myelin water quantification at 3 T.

Finally, the crucial role of accurate B_1 and B_0 imaging was revisited in chapter 5. A solution to simultaneous B_1 and B_0 mapping using a dual-echo actual flip angle imaging pulse sequence was presented. The suggested approach could successfully be applied to fast in vivo measurements and yielded reliable and robust maps.

Hence, the simultaneous B_1 and B_0 imaging technique might help to overcome systematic error sources in MWF mapping in the future.

In conclusion, this thesis presented novel myelin water imaging methods. Their applicability in a real clinical environment was intensely tested by incorporating in vivo measurements of healthy volunteers and multiple sclerosis patients. Moreover, possible influences that impair reliable myelin water detections were discussed in detail and solutions to circumvent limitations were proposed.

6.2 Outlook

Future work will be focused on establishing the methods proposed in this thesis in a clinical environment. Regrettably, the bSSFP measurements will not be pursued due to the too cumbersome analysis procedure and the strong dependence of the myelin water fraction on the fixed two-pool parameters. The emphasis will therefore be laid on the 3D mGRE acquisition at 1.5 T, because this procedure proved to be the most promising for accurate myelin water imaging.

An increased population of healthy subjects and multiple sclerosis patients has to be explored to clarify the possibility of characterizing MS lesions with the myelin water quantification technique based on 3D mGRE pulse sequences. Also a comparison to histopathology would be highly desirable to study the correlation between derived myelin water values and myelin staining results. In addition, possibilities to further increase the signal-to-noise ratios in the 1.5 T mGRE data will be investigated (like the application of improved 3D filters), because the stability of the analysis procedure and the myelin water results demonstrated a high sensitivity to noise present in the data.

Beyond that, quantifying myelin water proved to be feasible in the spinal cord, as it was shown by animal and human in vivo studies [35, 43, 44, 57]. The application of the 3D mGRE technique in the spinal cord would be conceivable, however an improved manual shimming method would then be required to correct for strong arising B_0 inhomogeneities.

Only lately, Deligianni et al. presented a modified version of the 3D mGRE pulse sequence that is based on a dynamic reduction of echo times towards the k-space center and a high asymmetric readout [87]. As a result, the first echo and the echo spacing could be reduced significantly and a comparable contrast to ultra-short TE sequences could be achieved. This approach benefits from allowing the acquisition of multiple echoes and could improve the accurate detection of the decreased T_2^* values of myelin water at 3 T in the future. In fact, a collaboration with Deligianni et al. is evolving at the moment and the application of the modified mGRE sequence for enhanced myelin water quantification is planned.

The simultaneous B_1 and B_0 mapping technique using dual-echo actual flip angle imaging is ready for use in the clinical routine. Because of the simple online postprocessing scheme that enables the direct visualization on the scanner console, the introduced fast procedure will soon be incorporated in clinical and research studies.

Hopefully, the work that was done during this Ph.D. will be useful for both basic research and clinics and the developed myelin water techniques will expand the knowledge of quantitative myelin water properties.

References

[1] Damadian R. Tumor detection by nuclear magnetic resonance. *Science*, 171:1151–1153, 1971.

[2] Lauterbur PC. Image formation by induced local interactions: Examples employing nuclear magnetic resonance. *Nature*, 242:190–191, 1973.

[3] Tofts P. Quantitative MRI of the brain: measuring changes caused by disease. *John Wiley & Sons Ltd.*, 2003.

[4] Provencher SW. A Fourier method for the analysis of exponential decay curves. *Biophys J*, 16:27–41, 1976.

[5] Vasilescu V, Katona E, Simplâceanu V, Demco D. Water compartments in the myelinated nerve. III. Pulsed NMR result. *Cell Mol Life Sci*, 34:1443–1444, 1978.

[6] Fischer HW, Rinck PA, van Haverbeke Y, Muller RN. Nuclear relaxation of human brain gray and white matter: Analysis of field dependence and implications for MRI. *Magn Reson Med*, 16:317–334, 1990.

[7] Menon RS, Allen PS. Application of continuous relaxation time distributions to the fitting of data from model systems and excised tissue. *Magn Reson Med*, 20:214–227, 1991.

[8] Laule C, Vavasour IM, Kolind SH, Li DKB, Traboulsee TL, Moore GRW, MacKay AL. Magnetic resonance imaging of myelin. *Neurotherapeutics*, 4:460–484, 2007.

[9] MacKay AL, Whittall KP, Adler J, Li DKB, Paty DW, Graeb DA. In vivo visualization of myelin water in brain by magnetic resonance. *Magn Reson Imaging*, 31:673–677, 1994.

[10] Does MD, Beaulieu C, Allen PS, Snyder RE. Multi-component T1 relaxation and magnetisation transfer in peripheral nerve. *Magn Reson Imaging*, 16:1033–1041, 1998.

[11] Does MD, Gore JC. Compartmental study of T1 and T2 in rat brain and trigeminal nerve in vivo. *Magn Reson Med*, 47:274–283, 2002.

[12] Bjarnason TA, Vavasour IM, Chia CLL, MacKay AL. Characterization of the NMR behavior of white matter in bovine brain. *Magn Reson Med*, 54:1072–1081, 2005.

[13] Deoni SCL, Rutt BK, Arun T, Pierpaoli C, Jones DK. Gleaning multicomponent T1 and T2 information from steady-state imaging data. *Magn Reson Med*, 60:1372–1387, 2008.

[14] Agre P, Preston GM, Smith BL, Jung JS, Raina S, Moon C, Guggino WB, Nielsen S. Aquaporin CHIP: the archetypal molecular water channel. *Am J Physiol*, 265:463–476, 1993.

[15] Koenig SH, Brown III RD, Spiller M, Lundbom N. Relaxometry of brain: Why white matter appears bright in MRI. *Magn Reson Med*, 14:482–495, 1990.

[16] Stanisz GJ, Kecojevic A, Bronskill MJ, Henkelman RM. Characterizing white matter with magnetization transfer and T2. *Magn Reson Med*, 42:1128–1136, 1999.

[17] Vavasour IM, Whittall KP, Li DKB, MacKay AL. Different magnetization transfer effects exhibited by the short and long T2 components in human brain. *Magn Reson Med*, 44:860–866, 2000.

[18] English AE, Whittall KP, Joy ML, Henkelman RM. Quantitative two-dimensional time correlation relaxometry. *Magn Reson Med*, 22:425–434, 1991.

[19] Laule C, Leung E, Li DK, Traboulsee AL, Paty DW, MacKay AL, Moore GR. Myelin water imaging in multiple sclerosis: quantitative correlations with histopathology. *Mult Scler*, 12:747–753, 2006.

[20] Gareau PJ, Rutt BK, Karlik SJ, Mitchell JR. Magnetization transfer and multicomponent T2 relaxation measurements with histopathologic correlation in an experimental model of MS. *J Magn Reson Imaging*, 11:586–595, 2000.

[21] Du YP, Chu R, Hwang D, Brown MS, Kleinschmidt-DeMasters BK, Singel D, Simon JH. Fast multislice mapping of the myelin water fraction using multicompartment analysis of T2* decay at 3T: A preliminary postmortem study. *Magn Reson Med*, 58:865–870, 2007.

[22] Laule C, Kozlowski P, Leung E, Li DKB, MacKay AL, Moore GRW. Myelin water imaging of multiple sclerosis at 7 T: Correlations with histopathology. *NeuroImage*, 40:1575–1580, 2008.

[23] Laule C, Vavasour IM, Leung E, Li DK, Kozlowski P, Traboulsee AL, Oger J, Mackay AL, Moore GR. Pathological basis of diffusely abnormal white matter: insights from magnetic resonance imaging and histology. *Mult Scler*, 17:144–150, 2011.

[24] Vavasour IM, Whittall KP, MacKay AL, Li DK, Vorobeychik G, Paty DW. A comparison between magnetization transfer ratios and myelin water percentages in normals and multiple sclerosis patients. *Magn Reson Med*, 40:763–768, 1998.

[25] Laule C, Vavasour IM, Moore GR, Oger J, Li DK, Paty DW, MacKay AL. Water content and myelin water fraction in multiple sclerosis. A T2 relaxation study. *J Neurol*, 251:284–293, 2004.

[26] Tozer DJ, Davies GR, Altmann DR, Miller DH, Tofts PS. Correlation of apparent myelin measures obtained in multiple sclerosis patients and controls from magnetization transfer and multicompartmental T2 analysis. *Magn Reson Med*, 53:1415–1422, 2005.

[27] Oh J, Han ET, Lee MC, Nelson SJ, Pelletier D. Multislice brain myelin water fractions at 3T in multiple sclerosis. *J Neuroimaging*, 17:156–163, 2007.

[28] Vavasour IM, Laule C, Li DK, Oger J, Moore GR, Traboulsee A, MacKay AL. Longitudinal changes in myelin water fraction in two MS patients with active disease. *J Neurol Sci*, 276:49–53, 2009.

[29] Levesque IR, Giacomini PS, Narayanan S, Ribeiro LT, Sled JG, Arnold DL, Pike GB. Quantitative magnetization transfer and myelin water imaging of the evolution of acute multiple sclerosis lesions. *Magn Reson Med*, 63:633–640, 2010.

[30] Flynn SW, Lang DJ, MacKay AL, Goghari V, Vavasour IM, Whittall KP, Smith GN, Arango V, Mann JJ, Dwork AJ, Falkai P, Honer WG. Abnormalities of myelination in schizophrenia detected in vivo with MRI, and postmortem with analysis of oligodendrocyte proteins. *Mol Psychiatry*, 8:811–820, 2003.

[31] Sirrs SM, Laule C, Madler B, Brief EE, Tahir SA, Bishop C, MacKay AL. Normal-appearing white matter in patients with phenylketonuria: water content, myelin water fraction, and metabolite concentrations. *Radiology*, 242:236–243, 2007.

[32] Wolff SD, Balaban RS. Magnetization transfer contrast (MTC) and tissue water proton relaxation in vivo. *Magn Reson Med*, 10:135–144, 1989.

[33] Dousset V, Grossman RI, Ramer KN, Schnall MD, Young LH, Gonzalez-Scarano F, Lavi E, Cohen JA. Experimental allergic encephalomyelitis and multiple sclerosis: lesion characterization with magnetization transfer imaging. *Radiology*, 182:483–491, 1992.

[34] Morrison C, Henkelman RM. A model for magnetization transfer in tissues. *Magn Reson Med*, 33:475–482, 1995.

[35] McCreary CR, Bjarnason TA, Skihar V, Mitchell JR, Yong VW, Dunn JF. Multiexponential T2 and magnetization transfer MRI of demyelination and remyelination in murine spinal cord. *Neuroimage*, 45:1173–1182, 2009.

[36] Whittall KP, MacKay AL, Graeb DA, Nugent RA, Li DKB, Paty DW. In vivo measurement of T2 distributions and water contents in normal human brain. *Magn Reson Med*, 37:34–43, 1997.

[37] Poon CS, Henkelman RM. Practical T2 quantitation for clinical applications. *J Magn Reson Imaging*, 2:541–553, 1992.

[38] Meiboom S, Gill D. Modified spin-echo method for measuring nuclear relaxation times. *Rev Sci Instrum*, 29:688, 1958.

[39] Levitt MH, Freeman R. NMR population inversion using a composite pulse. *J Magn Reson*, 33:473, 1979.

[40] Lawson CL, Hanson RJ. Solving least squares problems. *Englewood Cliffs: Prentice-Hall*, 1974.

[41] Whittall KP, MacKay AL. Quantitative interpretation of NMR relaxation data. *J Magn Reson*, 84:134–152, 1989.

[42] Fenrich FR, Beaulieu C, Allen PS. Relaxation times and microstructures. *NMR Biomed*, 14:133–139, 2001.

[43] Kozlowski P, Raj D, Liu J, Lam C, Yung AC, Tetzlaff W. Characterizing white matter damage in rat spinal cord with quantitative MRI and histology. *J Neurotrauma*, 25:653–676, 2008.

[44] Kozlowski P, Liu J, Yung AC, Tetzlaff W. High-resolution myelin water measurements in rat spinal cord. *Magn Reson Med*, 59:796–802, 2008.

[45] MacKay AL, Laule C, Vavasour IM, Bjarnason TA, Kolind S, Madler B. Insights into brain microstructure from the T2 distribution. *Magn Reson Imaging*, 24:515–525, 2006.

[46] Scheffler K, Lehnhardt S. Principles and applications of balanced SSFP techniques. *European Radiology*, 13:2409–2418, 2003.

[47] Carr HY. Steady-state free precession in nuclear magnetic resonance. *Phys Rev*, 112:1693–1701, 1958.

[48] Bloch F. Nuclear induction. *Phys Rev*, 70:460–474, 1946.

[49] Freeman R, Hill HDW. Phase and intensity anomalies in fourier transform NMR. *J Magn Reson*, 4:366–383, 1971.

[50] Zur Y, Stokar S, Bendel P. An analysis of fast imaging sequences with steady-state transverse magnetization refocusing. *Magn Reson Med*, 6:175–193, 1988.

[51] Haacke EM, Brown RW, Thompson MR, Venkatesan R. Magnetic resonance imaging: Physical principles and sequence design. *New York: John Wiley and Sons, Inc.*, 1999.

[52] Zur Y, Wood ML, Neuringer LJ. Spoiling of transverse magnetization in steady-state sequences. *Magn Reson Med*, 21:251–263, 1991.

[53] Ernst RR, Bodenhausen G, Wokaun A. Principles of nuclear magnetic resonance in one and two dimensions. *Oxford: Clarendon Press*, 1987.

[54] Holland J. Adaptation in natural and artificial systems. *Ann Arbor: University of Michigan Press*, 1975.

[55] Nelder JA, Mead R. A simplex method for function minimization. *Comput J*, 7:308–313, 1964.

[56] Kitzler HH, Su J, Zeineh M, Harper-Little C, Leung A, Kremenchutzky M, Deoni SC, Rutt BK. Deficient MWF mapping in multiple sclerosis using 3D whole-brain multi-component relaxation MRI. *Neuroimage*, [Epub ahead of print], 2011.

[57] Kolind SH, Deoni SC. Rapid three-dimensional multicomponent relaxation imaging of the cervical spinal cord. *Magn Reson Med*, 65:551–556, 2011.

[58] Lancaster JL, Andrews T, Hardies LJ, Dodd S, Fox PT. Three-pool model of white matter. *J Magn Reson Imaging*, 17:1–10, 2003.

[59] Trevor A, Lancaster JL, Dodd SJ, Contreras-Sesvold C, Fox PT. Testing the three-pool white matter model adapted for use with T2 relaxometry. *Magn Reson Med*, 54:449–454, 2005.

[60] Hwang D, Kim DH, Du YP. In vivo multi-slice mapping of myelin water content using T2* decay. *Neuroimage*, 52:198–204, 2010.

[61] Oppelt A, Graumann R, Barfuss H, Fischer H, Hartl W, Schajor W. FISP: eine neue schnelle Pulssequenz für die Kernspintomographie. *Electromedia*, 54:15–18, 1986.

[62] Gloor M, Scheffler K, Bieri O. Quantitative magnetization transfer imaging using balanced SSFP. *Magn Reson Med*, 60:691–700, 2008.

[63] Deoni SCL, Rutt BK, Jones DK. Investigating exchange and multicomponent relaxation in fully-balanced steady-state free precession imaging. *J Magn Reson Imaging*, 27:1421–1429, 2008.

[64] Jaynes ET. Matrix treatment of nuclear induction. *Phys Rev*, 98:1099–1105, 1955.

[65] Bieri O, Scheffler K. On the origin of apparent low tissue signals in balanced SSFP. *Magn Reson Med*, 56:1067–1074, 2006.

[66] Bieri O, Scheffler K. Optimized balanced steady-state free precession magnetization transfer imaging. *Magn Reson Med*, 58:511–518, 2007.

[67] Akoka S, Franconi F, Seguin F, Le Pape A. Radiofrequency map of an NMR coil by imaging. *Magn Reson Imaging*, 11:437–441, 1993.

[68] Smith SM, Jenkinson M, Woolrich MW, Beckmann CF, Behrens TEJ, Johansen-Berg H, Bannister PR, De Luca M, Drobnjak I, Flitney DE, Niazy RK, Saunders J, Vickers J, Zhang Y, De Stefano N, Brady JM, Matthews PM. Advances in functional and structural MR image analysis and implementation as FSL. *Neuroimage*, 23:208–219, 2004.

[69] Cox RW. AFNI: Software for analysis and visualization of functional magnetic resonance neuroimages. *Comput Biomed Res*, 29:162–173, 1996.

[70] Bieri O, Scheffler K. SSFP signal with finite RF pulses. *Magn Reson Med*, 62:1232–1241, 2009.

[71] Oh J, Han ET, Pelletier D, Nelson SJ. Measurement of in vivo multi-component T2 relaxation times for brain tissue using multi-slice T2 prep at 1.5 and 3 T. *Magn Reson Imaging*, 24:33–43, 2006.

[72] Pohmann R, von Kienlin M, Haase A. Theoretical evaluation and comparison of fast chemical shift imaging methods. *J Magn Reson*, 129:145–160, 1997.

[73] Huang T, Yang G, Tang G. A fast two-dimensional median filtering algorithm. *IEEE Trans Acoust Speech Signal Process*, 1:13–18, 1979.

[74] Bernstein MA, King KF, Zhou JZ. Handbook of MRI pulse sequences. *Elsevier Academic Press*, 2004.

[75] Graham SJ, Stanchev PL, Bronskill MJ. Criteria for analysis of multicomponent tissue T2 relaxation data. *Magn Reson Med*, 35:370–378, 1996.

[76] Kolind SH, Madler B, Fischer S, Li DK, MacKay AL. Myelin water imaging: Implementation and development at 3.0T and comparison to 1.5T measurements. *Magn Reson Med*, 62:106–115, 2009.

[77] Yablonskiy DA. Quantitation of intrinsic magnetic susceptibility-related effects in a tissue matrix. Phantom study. *Magn Reson Med*, 39:417–428, 1998.

[78] Reichenbach JR, Venkatesan R, Yablonskiy DA, Thompson MR, Lai S, Haacke EM. Theory and application of static field inhomogeneity effects in gradient-echo imaging. *J Magn Reson Imaging*, 7:266–279, 1997.

[79] Frahm J, Merboldt KD, Hanicke W. Direct FLASH MR imaging of magnetic field inhomogeneities by gradient compensation. *Magn Reson Med*, 6:474–480, 1988.

[80] Fernandez-Seara MA, Wehrli FW. Postprocessing technique to correct for background gradients in image-based R*(2) measurements. *Magn Reson Med*, 44:358–366, 2000.

[81] Constable RT, Spencer DD. Composite image formation in z-shimmed functional MR imaging. *Magn Reson Med*, 42:110–117, 1999.

[82] Posse S, Shen Z, Kiselev V, Kemna LJ. Single-shot T(2)* mapping with 3D compensation of local susceptibility gradients in multiple regions. *Neuroimage*, 18:390–400, 2003.

[83] Amadon A, Boulant N. Simultaneous measurement of B0- and B1-maps with modified actual flip angle imaging sequence. *Proc Intl Soc Magn Reson Med 16*, 2008.

[84] Santini F, Patil S, Scheffler K. IceLuva: A scripting framework for MR image reconstruction based on free software. *Concepts Magn Reson Part B*, 39B:1–10, 2011.

[85] Yarnykh VL. Actual flip-angle imaging in the pulsed steady state: a method for rapid three-dimensional mapping of the transmitted radiofrequency field. *Magn Reson Med*, 57:192–200, 2007.

[86] Nehrke K. On the steady-state properties of actual flip angle imaging (AFI). *Magn Reson Med*, 61:84–92, 2009.

[87] Deligianni X, Scheffler K, Bieri O. A high-resolution variable echo time 3D spoiled gradient echo sequence for imaging of short T2 components. *Proc Eur Soc Magn Reson Med Biol 28*, 2011.

Acknowledgements

I owe deep gratitude to

... my advisor Klaus Scheffler for providing his insight and assistance and for, most importantly, having trust in my pathway and my ideas,

... my supervisor Markus Klarhöfer for always helping me with the technical details of MR and for programming the mGRE pulse sequences,

... my co-examiner Stefan Ropele for being willing to evaluate this thesis and for truly always answering my e-mails within five minutes,

... Francesco Santini for guiding me with his deep insight into sequence programming and for being the best office mate ever,

... Xeni Deligianni for always trying to cheer me up and for her unstoppable pushing to participate in university sports,

... Monika Gloor for various discussions on one-, two- and three-pool models and steady state equations,

... all my colleagues from the Radiological Physics group for being willing to do coffee breaks at any time,

... Gregor Sommer, a clinical collaborator, who always showed great enthusiasm in studying diffusion weighted imaging in various patient groups,

... Ludwig Kappos, Julia Reinhardt and Christoph Stippich from the University of Basel Hospital for providing access to MS patients,

... the Swiss National Science Foundation and Bayer Schering Pharma Switzerland for financial support,

... my family for always encouraging me to stay in a gender-untypical field of study,

... and of course Christoph Kasper for being there for me at any time and for always motivating me when I felt lost (again).

Curriculum vitae

Personal data

Name:	Claudia Lenz
Date of birth:	28th of February, 1984
Place of birth:	Olten SO
Place of citizenship:	Uesslingen-Buch TG

Education

Sept. 2008 - Nov. 2011:	PhD in Biophysics
	University of Basel
	Supervisor: Prof. Dr. Klaus Scheffler
Oct. 2006 - Aug. 2008:	Master of Science in Physics
	University of Basel
Oct. 2003 - Oct. 2006:	Bachelor of Science in Physics
	University of Basel
Aug. 1996 - Sept. 2003:	Grammar school Olten SO
	Higher education entrance qualification
	Main subjects mathematics and natural sciences